

RESEARCH ARTICLE

10.1002/2016JB013237

Key Points:

- Lithospheric scale *S* wave velocity model for the northern Central Andean Plateau
- We image a well-resolved subducting Nazca slab and anisotropic Brazilian cratonic lithosphere
- Fast-velocity anomaly below the Altiplano suggests a geodynamic connection with modern topography

Supporting Information:

- Supporting Information S1

Correspondence to:

K. M. Ward,
kevin.m.ward@utah.edu

Citation:

Ward, K. M., G. Zandt, S. L. Beck, L. S. Wagner, and H. Tavera (2016), Lithospheric structure beneath the northern Central Andean Plateau from the joint inversion of ambient noise and earthquake-generated surface waves, *J. Geophys. Res. Solid Earth*, 121, 8217–8238, doi:10.1002/2016JB013237.

Received 3 JUN 2016

Accepted 1 NOV 2016

Accepted article online 5 NOV 2016

Published online 25 NOV 2016

Lithospheric structure beneath the northern Central Andean Plateau from the joint inversion of ambient noise and earthquake-generated surface waves

Kevin M. Ward^{1,2}, George Zandt², Susan L. Beck², Lara S. Wagner³, and Hernando Tavera⁴

¹Department of Geology and Geophysics, University of Utah, Salt Lake City, Utah, USA, ²Department of Geosciences, University of Arizona, Tucson, Arizona, USA, ³Department of Terrestrial Magnetism, Carnegie Institution of Washington, Washington, District of Columbia, USA, ⁴Instituto Geofísico del Perú, Lima, Peru

Abstract The Central Andean Plateau (CAP), as defined by elevations in excess of 3 km, extends over 1800 km along the active South American Cordilleran margin making it the second largest active orogenic plateau on Earth. The uplift history of this high Plateau, with an average elevation around 4 km above sea level, remains uncertain as paleoelevation studies along the CAP suggest a complex, nonuniform uplift history. As part of the Central Andean Uplift and the Geodynamics of High Topography (CAUGHT) project, we image the *S* wave velocity structure of the crust and upper mantle using surface waves measured from ambient noise and teleseismic earthquakes to investigate the upper mantle component of plateau uplift. We observe three main features in our *S* wave velocity model including (1) a positive velocity perturbation associated with the subducting Nazca slab; (2) a negative velocity perturbation below the sub-Andean crust that we interpret as anisotropic Brazilian cratonic lithosphere; and (3) a high-velocity feature in the mantle above the slab that extends along the length of the Altiplano from the base of the Moho to a depth of ~120 km. A strong spatial correlation exists between the lateral extent of this high-velocity feature and the relatively lower elevations of the Altiplano basin suggesting a potential relationship. Determining if this high-velocity feature represents a small lithospheric root or foundering of orogenic lithosphere requires more integration of observations, but either interpretation implies a strong geodynamic connection with the uppermost mantle and the current topography of the northern CAP.

1. Introduction and Tectonic Background

The central Andes of southern Peru, Bolivia, Argentina, and Chile (between 14°S and 28°S) define the type example of an active Cordilleran orogen where tectonics are driven by normal-dipping, obliquely converging subduction of the oceanic Nazca Plate beneath the continental South American Plate [Barazangi and Isacks, 1976; Cahill and Isacks, 1992; Norabuena et al., 1998; Kendrick et al., 2003]. Commensurate with the subduction of hydrated oceanic lithosphere, abundant arc and intra-arc volcanism is observed along the South American margin where volcanic quiescence associated with present-day flat-slab subduction geometries have partitioned active arc volcanic activity into northern, central, and southern volcanic zones [James, 1971; Jordan et al., 1983; Ranero and Sallares, 2004; Ramos and Folguera, 2009; Hayes et al., 2012]. The Central Volcanic Zone (CVZ, between 14°S and 28°S) is a collection of andesitic to dacitic stratovolcanoes, regionally extensive and voluminous crystal-rich dacitic ignimbrites, and minor small-volume monogenetic mafic centers [de Silva, 1989; Francis and de Silva, 1989; Davidson and de Silva, 1992] truncated to the north by Peruvian (11 Ma to present) flat-slab subduction and in the south by Pampean (12 Ma to present) flat-slab subduction [Cahill and Isacks, 1992; Ramos and Folguera, 2009]. Along this stretch of the South American Cordillera, the orogen attains its greatest width and highest average elevation, forming the largest high plateau in the world associated with abundant arc magmatism, the Central Andean Plateau (CAP) [Allmendinger et al., 1997].

The CAP, as defined by the 3 km elevation contour, extends over 1800 km along the active continental Cordilleran margin reaching a maximum width around 400 km near the Bolivian Orocline (Figure 1) making it second only to the Tibetan Plateau in geographic extent [Allmendinger et al., 1997]. In the core of the CAP is the low-relief internally drained Altiplano (north) and the high-relief Puna (south) bounded to the west by the Western Cordillera, the active volcanic arc, and to the east by the Eastern Cordillera, an inactive basement-cored fold-and-thrust belt. In the northernmost section of the CAP, the Altiplano narrows before terminating north of Lake Titicaca in southern Peru. The flanks of the CAP are buttressed to the west by one of the largest

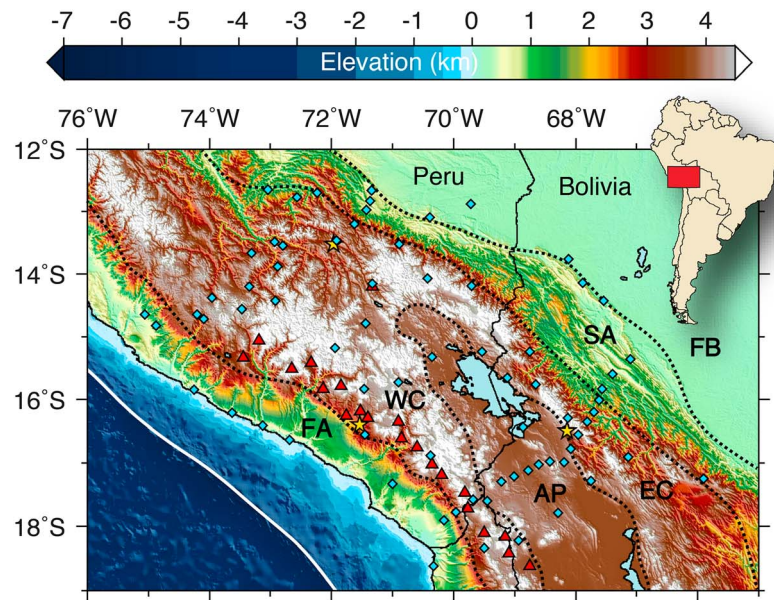


Figure 1. Map of study area with the location of broadband seismic stations shown as blue diamonds. Red triangles show Holocene volcanic activity, and morphotectonic provinces are separated by dashed black lines (FA, fore arc; WC, Western Cordillera; AP, Altiplano; EC, Eastern Cordillera; SA, sub-Andes; FB, foreland basin).

monoclines on Earth likely due to west-vergent thrusting beneath the Western Cordillera [e.g., *Victor et al.*, 2004; *Armijo et al.*, 2015] and to the east by the active east-vergent fold-and-thrust belt of the sub-Andes [e.g., *Baby et al.*, 1995, 1997; *Kley*, 1999; *McQuarrie et al.*, 2005]. Recent tectonic interpretations thus see the central Andes and the CAP as a bivergent orogen with more or less importance given to west and east verging thrusting [e.g., *Armijo et al.*, 2015; *Lamb*, 2015].

Despite the Plateau's impact on the dynamic evolution of the South American Cordillera [*Barnes and Ehlers*, 2009, and references therein], first-order questions about principal segments of the current lithospheric structure beneath the northern CAP remain unanswered and a comprehensive model for the enigmatic uplift history of the plateau remains tenuous. Three tectonic processes have emerged as possible mechanisms for the Plateau's uplift: (1) slow and steady uplift due either to protracted underthrusting of the Brazilian shield and shortening of the eastern plateau [e.g., *Jordan et al.*, 1997; *Lamb*, 2011] or to a progressive migration of crustal shortening from west to east across the whole orogen over the last 50 Myr [e.g., *Elger et al.*, 2005; *Armijo et al.*, 2015]; (2) rapid uplift associated with isostatic rebound following delamination of the lower Altiplano-Puna crust [e.g., *Garzzone et al.*, 2008]; and (3) thickening of the Altiplano crust through mid/lower crustal flow possibly augmented by magmatic addition or underplating [e.g., *Husson and Sempere*, 2003]. Although a review of the evidence for and against each of these proposed mechanisms' contribution to the uplift history is beyond the scope of this study [see *Barnes and Ehlers*, 2009; *Saylor and Horton*, 2014], each of the proposed uplift mechanisms makes specific predictions about the current lithospheric structure. A well-resolved lithospheric scale *S* wave velocity model in combination with other geological/geophysical studies can be used to help differentiate between different proposed uplift mechanisms. For example, (1) fast seismic velocities in the lower crust extending eastward into cratonic South America would support uplift driven by underthrusting of the Brazilian shield [e.g., *Ma and Clayton*, 2015]; (2) anomalously fast seismic velocities in the uppermost mantle would suggest foundering of the lithosphere driving rapid surface uplift [e.g., *Calixto et al.*, 2013]; and (3) a midcrustal low-velocity zone might indicate the presence of a weak crust capable of ductile flow [e.g., *Liu et al.*, 2014]. Future work that incorporates receiver functions into a joint inversion will provide additional details on the crustal structure, facilitating a better examination of the relative contributions from underthrusting and crustal flow as surface uplift mechanisms. As our data set and method provides continuous high-resolution *S* wave velocity results in the uppermost mantle below the northern CAP, we focus our interpretation on (1) the isostatic/geodynamic effect of the mantle anomalies we observe on modern surface topography and (2) the tectonic processes consistent with generating the observed anomalies in the uppermost mantle.

2. Data and Methods

In the last decade, advancements in measuring surface wave dispersion (SWD) from earthquake-generated surface waves and empirical Green's functions (EGFs) extracted from the ambient seismic wavefield have allowed the crust and lithospheric mantle to be imaged in previously unavailable detail. The two-plane wave tomography (TPWT) method used in this study helps reduce the systematic biasing effects of scattering and multipathing in the incoming wavefield ignored by single-plane wave approaches to measure SWD from earthquake-generated surface waves [Forsyth *et al.*, 1998; Forsyth and Li, 2005]. TPWT has been especially successful in imaging the lower crust and upper mantle along the American Cordillera because of the method's ability to measure longer period surface waves that are sensitive to the lower crust and uppermost mantle, typically in the period range of 20–143 s [Wagner *et al.*, 2010a; Gilbert *et al.*, 2012; Calixto *et al.*, 2013; Antonijevic *et al.*, 2015]. The ambient noise tomography (ANT) method we employ uses the cross correlation of ambient seismic noise to extract EGFs for the path between two seismic stations [Sabra *et al.*, 2005; Shapiro *et al.*, 2005]. The EGFs are subsequently used in a frequency time analysis (FTAN) to measure the interstation SWD typically in the period range of 8–50 s, although emerging work suggests that this approach may successfully be extended to measure longer periods [Yang, 2014]. This relaxes the limitations imposed by the often nonuniform spatial and temporal distribution of earthquakes that can bias or streak tomographic results provided that sufficient continuous data are available to extract robust EGFs [Bensen *et al.*, 2007]. ANT has been especially successful in imaging the shallow crust at local to continental scales [Lin *et al.*, 2007; Yang *et al.*, 2007; Bensen *et al.*, 2008; Zheng *et al.*, 2008; Saygin and Kennett, 2010; Yang *et al.*, 2010; Ward *et al.*, 2013; Delph *et al.*, 2015] because it does not use earthquake-generated surface waves that attenuate rapidly at periods that are primarily sensitive to the shallow crust (<20 s). Since the ANT and TPWT methods are in principle sensitive to the same rock properties of the solid Earth, combining the two methods to produce SWD measurements in the period range of 8–143 s has become a popular approach for investigating the whole lithospheric structure [Yang *et al.*, 2011; Porter *et al.*, 2012; Wagner *et al.*, 2012; Ma and Clayton, 2014]. In the following sections, we briefly describe the details of the TPWT and ANT methods and our approach of combining them into a joint inversion for the 3-D *S* wave velocity structure of the northern CAP.

2.1. Ambient Noise Tomography

In a previous study, Ward *et al.* [2013] used the vertical component from 330 broadband seismic sensors across much of the central Andes to measure the dispersion of Rayleigh waves in the period range of 8–50 s from ambient seismic noise. The specific details of processing the raw waveforms and extracting interstation dispersion curves are described by Ward *et al.* [2013, and references therein], and we refer the interested reader to that reference for more information. As an intermediate step in the ANT method, Ward *et al.* [2013] inverted the extracted interstation dispersion measurements into a uniformly gridded 2-D phase velocity model with geographic grid spacing of $0.1^\circ \times 0.1^\circ$ for each of the 13 periods measured (8–50 s). The TPWT method requires a 2-D phase velocity starting model, and we use the ANT results as a priori information in constructing the starting model. For our particular data set, however, using the ANT phase velocity maps sampled at $0.1^\circ \times 0.1^\circ$ precludes resolving statistically meaningful TPWT results, and therefore, we have generated new 2-D phase velocity maps [Barmin *et al.*, 2001] using a coarser grid spacing of $0.25^\circ \times 0.25^\circ$ (Figure S1). Inverting the interstation dispersion curves with coarser grid spacing also allows us to evaluate the resolution of the new 2-D phase velocity maps (Figure S2).

2.2. Two-Plane Wave Tomography

The two-plane wave tomography method uses earthquake-generated surface waves by modeling the incoming wavefield as the superposition of two distinct interfering plane waves each with its own amplitude, phase, and back azimuth for a total of six parameters [Forsyth *et al.*, 1998; Forsyth and Li, 2005]. For our isotropic solution, the modeled phase and amplitude at each station (observations) are iteratively compared against the predicted values (initially calculated from the starting model and then subsequently from the previous iterations result), solving for the lateral 2-D phase velocity structure as a function of period. This approach helps reduce the systematic biasing effects of scattering and multipathing introduced into the incoming wavefield outside of our seismic arrays footprint [Wielandt, 1993]. Wavefield scattering introduced inside the footprint of our array is accounted for by using finite frequency kernels [Yang and Forsyth, 2006] based upon the single-scattering Born approximation [Zhou *et al.*, 2004]. Additional details common to the

TPWT method are presented by Forsyth and Li [2005]. In the following sections we discuss the processing details relevant to our specific TPWT analysis.

2.2.1. Data and Raw Waveform Processing

As part of the National Science Foundation (NSF) Continental Dynamics (CD) project: Central Andes Uplift and the Geodynamics of High Topography (CAUGHT) [Beck *et al.*, 2010; Ward *et al.*, 2013], we deployed 50 Streckeisen STS-2 broadband seismic sensors across the northern CAP in northern Bolivia and southern Peru (Figure 1). The CAUGHT temporary seismic deployment lasted approximately 2 years (from October 2010 to August 2012), and of the 51 CAUGHT stations/locations occupied during the deployment, 45 recorded waveforms used in this TPWT analysis. We augment the CAUGHT network with 16 stations from the Peru Lithosphere and Slab Experiment (PULSE) [Wagner *et al.*, 2010b; Eakin *et al.*, 2014] and 8 stations from the Peru Subduction Experiment (PeruSE) [Phillips *et al.*, 2012] temporary broadband seismic deployments. Two permanent stations from the Integrated Plate Boundary Observatory Chile (IPOC) [GFZ German Research Centre for Geosciences and Institut des Sciences de l'Univers-Centre National de la Recherche CNRS-INSU, 2006; Sodoudi *et al.*, 2011] and one station (LPZ) from the Global Telemetered Seismograph Network (USAF/USGS) [Albuquerque Seismological Laboratory [ASL]/USGS, 1993] were also added for a total of 72 broadband seismic stations. Our virtual array has an average station spacing of ~ 30 km enclosed in a $\sim 300,000$ km² footprint which is particularly well suited to lithospheric-scale tomographic studies.

The 66 events used in this study were selected from an epicentral distance range of 30–130° degrees from each station and have a body wave magnitude (M_b) of 5.5 or greater. Although the back azimuthal distribution of the events is biased from the southwest direction (Figure S3), we were able to record and use enough events from different back azimuths to prevent streaking in our results. We use the vertical component of the broadband sensors to measure the SWD of Rayleigh waves for 14 periods (25, 29, 33, 40, 45, 50, 59, 67, 77, 91, 100, 111, 125, and 143 s). Initial processing of the raw waveforms included applying a transfer function convolving all waveforms with the same third-generation Streckeisen STS-2 instrument response to preserve the relative amplitude of waveforms across the virtual array. The waveforms were then bandpass filtered using a four-pole, Butterworth filter with corner frequencies of 5 mHz above and below the 14 center frequencies of interest. For each of the event station pairs in the period range of 25–143 s, the event waveforms were visually inspected and windowed around the fundamental mode Rayleigh wave. Nearly 80% of the events that met the distance and magnitude criteria did not record useable waveforms or meet our 10:1 signal-to-noise (SNR) threshold yielding a total of 18,240 event station pairs across the 14 periods measured.

2.2.2. Model Resolution and Parameterization

Model resolution as expressed in lateral variations allowed during the inversion is in part controlled by an a priori covariance matrix of model standard deviations [Forsyth and Li, 2005]. Large values allow for more variation in the model but can introduce lateral oscillation instabilities into the results, whereas small values restrict the model's ability to deviate from the starting model. We use 0.1 km/s for the value of the a priori covariance matrix after evaluating the tradeoffs between model stability and model resolution. This value is sufficiently large enough so as to not restrict the inversion from fitting the observations while simultaneously preventing lateral instabilities in the model results. As expected, the a posteriori model standard deviations are lowest in the center of our array's footprint and increase with increasing period (Figure S4). Selection of grid spacing also has an effect on the stability and resolution of the inversion results and therefore warrants careful consideration.

For all periods measured in this TPWT study, we select a $0.25^\circ \times 0.25^\circ$ geographic grid spacing. Inverting for a grid with smaller spacing introduces short wavelength features potentially associated with larger model instability. Lateral resolution reaches a maximum around 50 s and gradually contracts for longer periods. The nonuniform distribution of earthquake magnitudes yields fewer quality waveforms at longer periods reducing the number of observations further contracting the lateral resolution (Figure S5). Parameterization of the model space is also extended several grid nodes ($>2^\circ$ of latitude and longitude) beyond our arrays footprint so that poorly modeled traveltime variations can be absorbed by the outermost nodes.

2.2.3. Phase Velocity Starting Model

Phase velocity results obtained using the TPWT method exhibit dependency on the starting model, and therefore, the selection of the starting model requires some justification. Quantifying this justification is, however, difficult, because phase velocity results obtained from different starting models can vary significantly (beyond two standard deviations) while yielding roughly consistent a posteriori model standard deviations

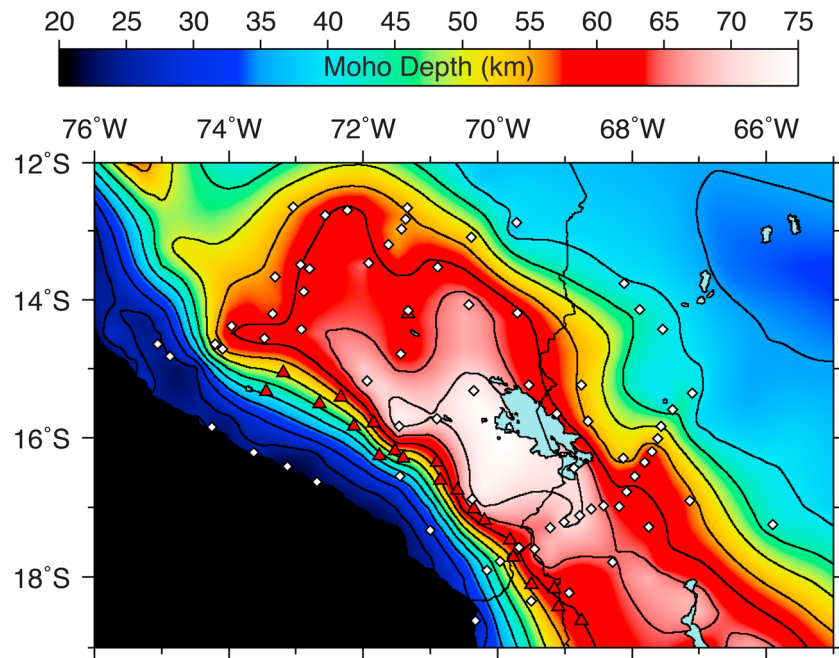


Figure 2. Map of depth to Moho used to generate starting model for the two-plane wave inversion. This map was generated using Moho measurements of <40 km from the model of *Tassara and Echaurren* [2012] and are combined with Moho measurements of >40 km determined from receiver function studies [*Ryan et al.*, 2016] and then interpolated on a regular $0.25^\circ \times 0.25^\circ$ grid using a natural neighbor algorithm.

and misfit [*Weeraratne et al.*, 2007]. Previous seismological studies reveal large lateral variations in both crustal velocity [*Ward et al.*, 2013] and thickness [*Beck and Zandt*, 2002; *Ryan et al.*, 2016] across our study area limiting the efficacy of a constant velocity starting model. Laterally constant 2-D starting velocity models are heavily penalized by the inversion in areas with lateral variations that exceed the a priori covariance matrix standard deviation resulting in reduced amplitude recovery. We therefore use the ANT results as a priori information in the form of a laterally variable 2-D starting model for the TPWT inversion. This helps constrain the TPWT inversion results by accounting for the large lateral velocity variations observed in the crust [*Ward et al.*, 2013]. The central Andes also have large lateral gradients in crustal thickness [*Beck and Zandt*, 2002; *Ryan et al.*, 2016] resulting in large lateral velocity variations that can contribute to the same model stability versus resolution tradeoffs if not accounted for in the starting model. Integrating Moho constraints into our 2-D starting model is not as trivial as addressing the inhomogeneous crustal velocity structure requiring a more complex approach to constructing a starting model.

Our approach involves constructing 1-D S wave velocity profiles for each grid point in our model using the S wave velocity model of *Ward et al.* [2013] for the crust, whereas the crustal thickness is constrained from a hybrid Moho integrating measurements from gravity and receiver functions studies [*Tassara and Echaurren*, 2012; *Ryan et al.*, 2016]. Moho measurements of <40 km are selected from the model of *Tassara and Echaurren* [2012] and are combined with Moho measurements of >40 km determined from receiver function studies [*Ryan et al.*, 2016] and then interpolated on a regular $0.25^\circ \times 0.25^\circ$ grid using the natural neighbor [*Sibson*, 1980, 1981] algorithm (Figure 2). We use the receiver function constraints where we believe they are more robust and rely on the gravity estimates where the receiver function data are either poorly sampled or unreliable due to complexities from basin reverberations or mantle hydration effects. These latter problems generally occur in the fore arc or on the edge of the back-arc basins where crustal thickness is less than ~ 40 km; hence, that depth is a convenient “marker” to distinguish the two sets of locations. At depths below the Moho where less a priori information is available, we use a modified ak135 Earth reference model to complete each 1-D profile [*Kennett et al.*, 1995]. Each 1-D S wave velocity profile is then forward modeled to produce an equivalent 1-D Rayleigh wave phase velocity dispersion curve consisting of the 14 periods used in this TPWT study [*Herrmann and Ammon*, 2004]. After arranging the phase velocities from the 1-D vertical

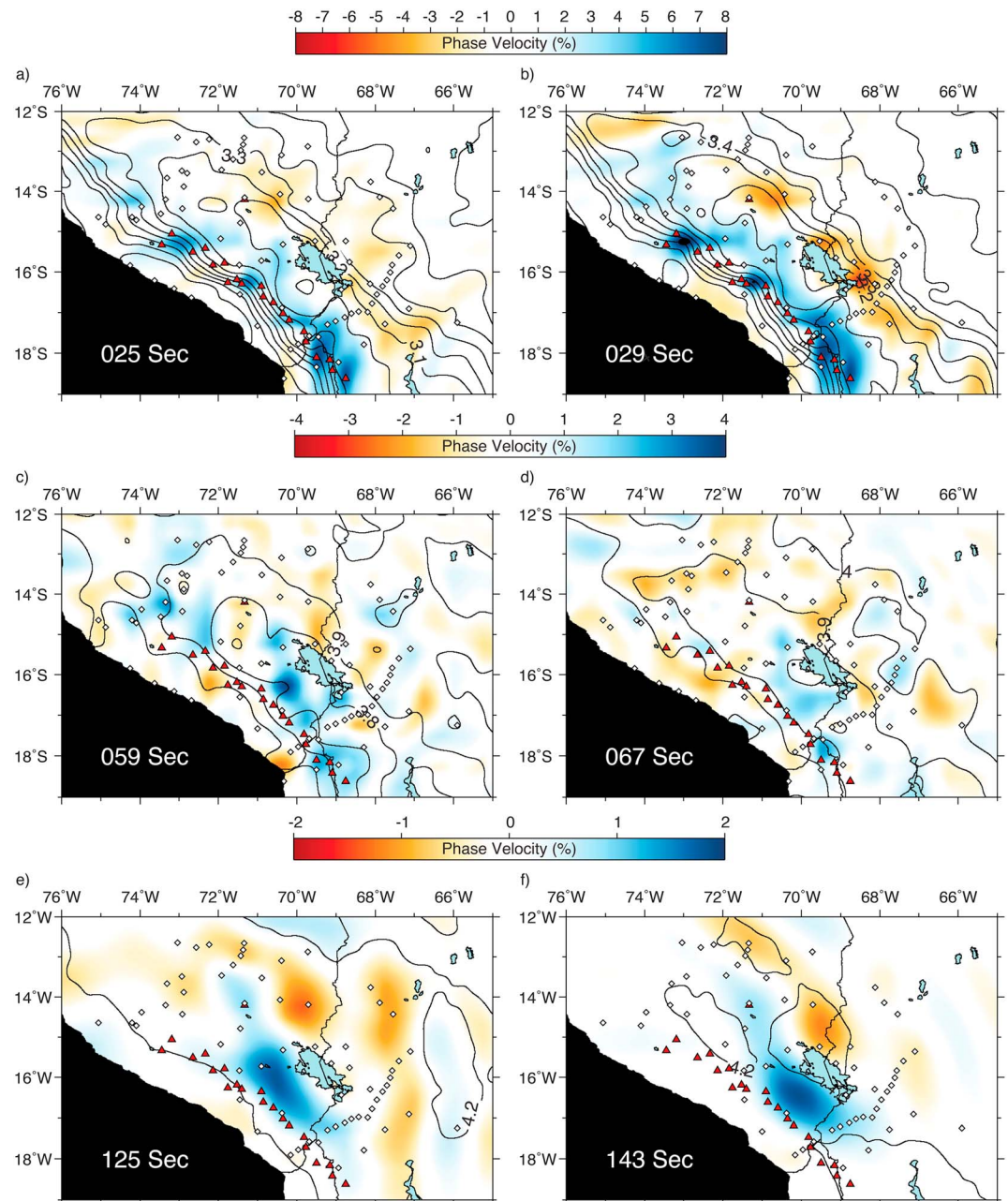


Figure 3. Map of phase velocities for 6 of the 14 periods measured using the two-plane wave tomography method. Velocities are shown as perturbations from the starting model used in the inversion with absolute velocities shown as contorted black lines.

profile into 14 two-dimensional horizontal slices, the laterally variable 2-D phase velocity maps are used as the starting model in the TPWT inversion thereby including as much a priori information as possible to generate well-constrained phase velocity results (Figures 3 and S6).

2.3. Integrating the ANT and TPWT Results

At six intermediate periods (25, 29, 33, 40, 45, and 50 s), the ANT and TPWT results overlap providing a comparative metric for establishing the robustness of dispersion measurements calculated from fundamentally different approaches. On average, the difference between the two methods is less than ~2% where there is good resolution. Although the two methods produce extremely consistent results within model uncertainties, in areas where the differences are large, averaging the overlapping results can introduce rough 1-D vertical

dispersion profiles not characteristic of real Earth models. This requires that we adopt a more sophisticated approach of integrating the ANT and TPWT results.

We take advantage of the observation that both methods have a period at which the number of raypaths (observations) peaks, decaying above and below that period. For the ANT method, the number of raypaths peaks around 18 s and at 50 s for the TPWT method. Using the number of raypaths as a relative proxy for resolution, we linearly scale the weighting of the overlapping phase velocity results so that the shorter intermediate periods are weighted more toward the ANT results and the longer intermediate periods are weighted more from the TPWT results. This approach helps to produce smooth 1-D dispersion profiles that reduce artifacts and instability in the subsequent *S* wave velocity inversion.

2.4. *S* Wave Velocity Inversion

In the Earth, Rayleigh waves are dispersive, meaning different periods are sensitive to different depths. Because surface waves have broad period-dependent sensitivity kernels, different periods have variably weighted overlapping sensitivity to the same velocity structure. By combining dispersion measurements made at shorter periods (8–50 s) from ambient noise with longer periods (25–143 s) generated by earthquakes, the overlapping sensitivity constrains the *S* wave velocity results better than independently using only surface wave dispersion generated from ambient noise or earthquakes. This is important for our study area where large variations in both crustal velocity [Ward *et al.*, 2013] and thickness [Beck and Zandt, 2002; Ryan *et al.*, 2016], not accounted for by averaged or global starting models, may introduce artifacts into the inversion results. At each $0.25^\circ \times 0.25^\circ$ grid location, we use a linearized iterative least squares approach to invert each 1-D phase velocity profile (8–143 s) into a 1-D *S* wave velocity model [Herrmann and Ammon, 2004]. During the *S* wave inversion, each of the 21 surface wave dispersion values are inversely weighted by the standard deviation of the TPWT results. As the ANT method does not produce a similar type standard deviation measurement, we weight the shorter ANT periods with the lowest standard deviation from the TPWT results for each specific 1-D dispersion profile.

2.4.1. Starting Model Parameterization and Uncertainties

In general, the largest vertical velocity contrasts are expected across the Moho with large intercrustal low-velocity zones being a rare exception [Ward *et al.*, 2014a]. *S* wave velocity inversions using only surface waves (without additional constraints) are not particularly well suited to imaging the depths and velocity contrasts of discontinuities, resulting in vertically smoothed 1-D velocity models. Since the broad period-dependent sensitivity kernels limit the resolution of vertical discontinuities, adding these discontinuities to the starting model helps to reduce vertical smoothing artifacts. We therefore include the Moho discontinuity (Figure 2) in our starting model and combined with the crustal model of Ward *et al.* [2013] constrain the larger lithospheric scale features we are interested in interpreting. However, uncertainties in the depths of the Moho and, to a lesser extent, the magnitude of the velocity contrast can alter the inversion results up to ~10 km above and below location of the input Moho [Stachnik *et al.*, 2008].

End member V_p/V_s ratios (1.70–1.80) and attenuation values (quality factor 50–500) in the crust have a very small effect (second order to starting *S* wave velocity, damping, and number of iterations) on the final *S* wave velocity models (see discussion in Ward *et al.* [2013, supporting information]). We choose a V_p/V_s ratio of 1.75 [Ryan *et al.*, 2016] and an average quality factor of 150 [Baumont *et al.*, 1999] in the crust transitioning to a V_p/V_s ratio of 1.78 in the mantle for all 1-D starting models. Surface waves are not sensitive to high-frequency (rapid vertical) changes in V_p/V_s or attenuation limiting the uncertainties in our model results associated with varying V_p/V_s ratios or attenuation values in our starting model. The thickness of each layer in the starting model is adjusted to accommodate a layer boundary at the Moho and dilates with depth to ensure that the diagonal of the resolution matrix for each layer is approximately between 0.1 and 0.3 over the depth range of interest (~200 km; Figure S7). After the inversion, crustal and mantle layers are independently smoothed using a smoothing spline and represent the results shown in the following section.

Our final *S* wave velocity results use the hybrid Moho constructed from gravity and receiver function studies [Tassara and Echaurren, 2012; Ryan *et al.*, 2016], the crustal velocity model of Ward *et al.* [2013], a modified ak135 Earth reference model in the mantle [Kennett *et al.*, 1995], a V_p/V_s ratio of 1.75 in the crust [Ryan *et al.*, 2016], a V_p/V_s ratio in the mantle of 1.78 [Kennett *et al.*, 1995], and a quality factor of 150 [Baumont *et al.*, 1999] in the crust. This starting model combined with a damping value of 0.5 and between 8 and 11

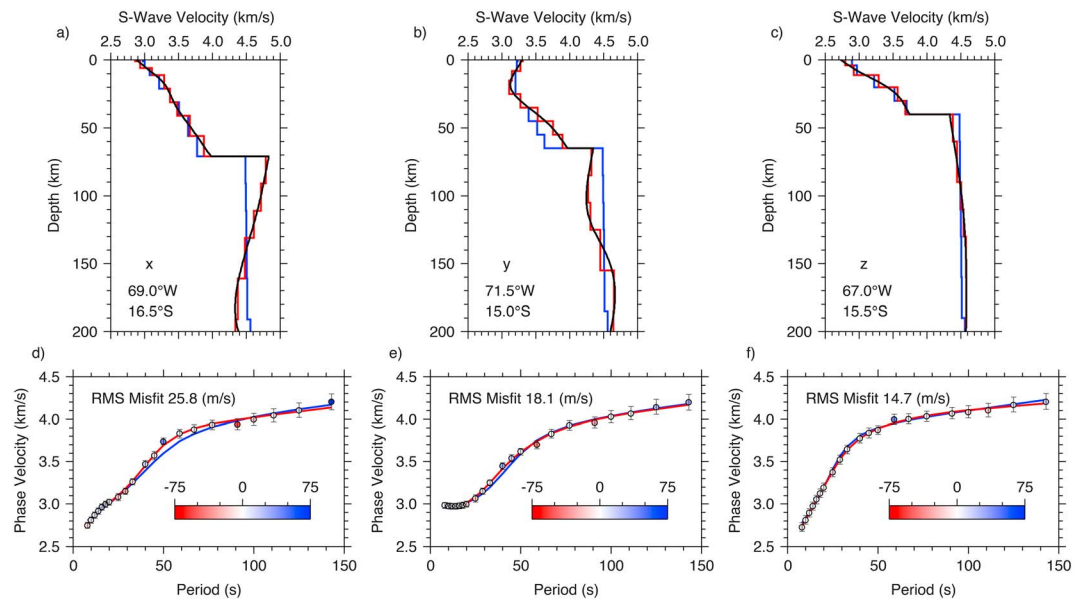


Figure 4. One-dimensional *S* wave velocity models and corresponding 1-D dispersion curves for three locations of tectonic significance (locations *x*, *y*, and *z* shown on Figure 5f as yellow circles). Starting models shown as blue lines with the final model shown with red lines (black lines show smoothed *S* wave velocity model). Dispersion data shown as open circles with one standard deviation error bars and deviation from final model shown as circle color fill (e.g., red circle fill indicates that dispersion data are lower than final model dispersion).

iterations produces a stable *S* wave velocity model containing robust features independent of the starting model fitting the dispersion data relatively well (Figure S8).

2.5. Density Modeling

Surface waves are primarily sensitive to the *S* wave velocity structure of the Earth, secondarily to the *P* wave velocity, and, to a lesser extent, the density and attenuation structure. Our method is not particularly sensitive enough to directly image the density structure within any acceptable uncertainty bounds; however, empirical relationships have been derived linking seismic *P* wave velocities to densities. Assuming a V_p/V_s ratio to convert our *S* wave measurements to *P* wave velocities, we use the Nafe-Drake curve [Ludwig et al., 1970] formalized by Brocher [2005] to model the density structure of our study area. Over the velocity range we are interested in modeling, Brocher's relationship models the bulk density structure of our study area sufficiently well over long wavelengths (>75 km). Small amounts of partial melt/fluids, temperature variations, and composition variations can add uncertainty into the absolute velocity-density empirical relationships; however, relative bulk density calculations are robust enough to warrant first-order consideration in our isostatic calculations. We note here that although we use a variable density model derived from Brocher's velocity-density relationship, our isostatic calculations are primarily sensitive to crustal thickness variations and, to a lesser extent, the density contrast across the crust/mantle boundary.

3. Results

Our *S* wave velocity model results are shown as three 1-D velocity profiles (Figure 4, locations shown in Figure 5f), six horizontal depth slices (Figure 5), and five vertical cross sections (Figure 6, locations shown in Figure 5f). Although our horizontal depth slices show results located outside the footprint of our array, we limit our interpretation of the model results to structures located inside the footprint of the array primarily because uncertainties in the phase velocity measurements rapidly increase outside of the array's footprint. In the cross sections, we plot the crust as absolute velocities and the mantle as velocity perturbations from the starting model, while emphasizing that the crust and mantle results are from the same 1-D inversion profile at each grid location in the model. The focus of this study is the uppermost mantle, and five large mantle velocity anomalies provide a natural descriptive organization described in the following sections.

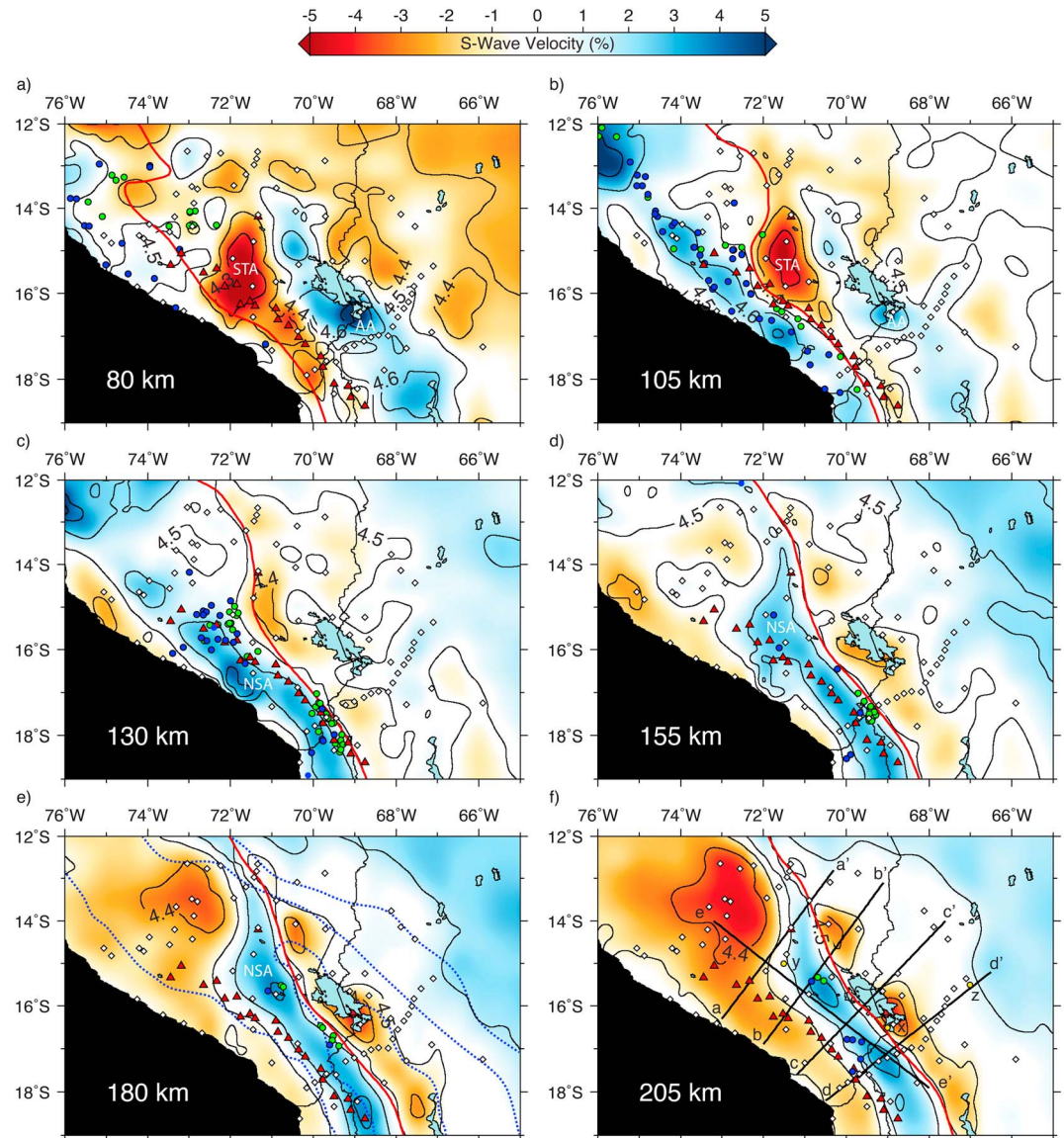


Figure 5. Two-dimensional horizontal *S* wave velocity results for six depth slices shown as perturbations from the starting model (starting model values for each depth slice is constant for the same depth slice shown). Red contour shows Slab 1.0 contours [Hayes *et al.*, 2012] for each corresponding depth slice. Green (circles) earthquake locations are from Kumar *et al.* [2016] and blue (circles) earthquake locations are from Instituto Geofísico del Perú. Morphotectonic provinces from Figure 1 are shown as blue dashed lines with the locations of three 1-D profiles (Figures 4a–4c) shown as yellow circles and the location of five 2-D cross-section slices (Figure 6) shown as black lines. NSA, Nazca slab anomaly; STA, sub-Moho slab transition anomaly; AA, sub-Moho Altiplano anomaly.

3.1. The Nazca Slab Anomaly

By including a priori information into our starting model, such as a well-constrained Moho interface and a crustal velocity structure, we image a relatively coherent slab anomaly across most of our model space that is consistent with the predicted location based on slab earthquakes. Below ~80 km, the continuous slab anomaly (>2%) follows the Slab 1.0 contours [Hayes *et al.*, 2012] and the earthquake locations relatively well [Kumar *et al.*, 2016]. The apparent topography on the top of the slab (Figures 6b and 6c) and depression (Figure 6a) in the slab anomaly (relative to the Slab 1.0 contour) are almost certainly artifacts resulting from model smoothing integrating higher velocities above the slab topography examples (Figures 6b and 6c) and low velocities in the depressed slab anomaly example (Figure 6a). Above ~80 km, a similar apparent deflection/distortion of the slab anomaly below the fore arc (relative to the Slab 1.0 contour) is observed in

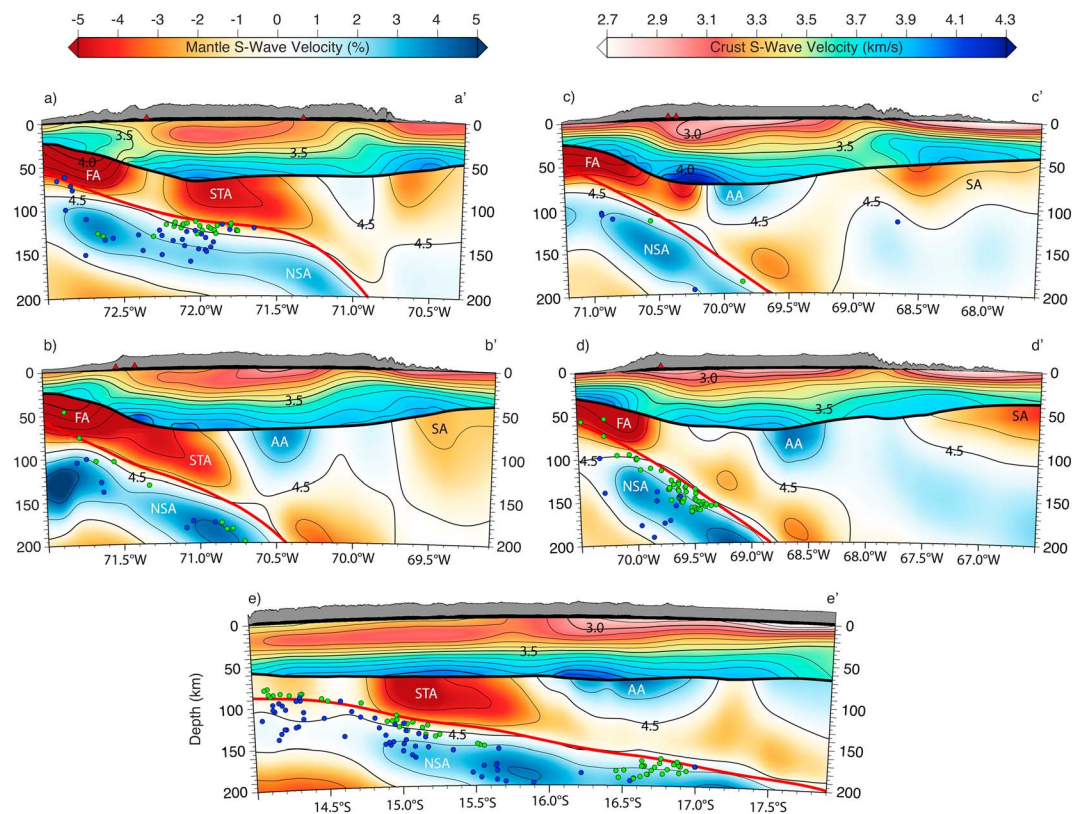


Figure 6. (a–d) Four trench-perpendicular and (e) one trench-parallel vertical S wave velocity cross sections from our model (locations shown in Figure 5f) shown as perturbations from the starting model in the mantle and absolute velocity in the crust. The Moho is shown as a thick black line (Figure 2), and the Slab 1.0 contours [Hayes *et al.*, 2012] are shown as a red line. Green (circles) earthquake locations are from Kumar *et al.* [2016], and blue (circles) earthquake locations are from Instituto Geofísico del Perú. NSA, Nazca slab anomaly; FA, sub-Moho fore-arc anomaly; STA, sub-Moho slab transition anomaly; SA, sub-Moho sub-Andean anomaly; AA, sub-Moho Altiplano anomaly.

all cross sections (Figure 6). This apparent deflection/distortion of the slab anomaly above ~80 km is characteristic of a reduced velocity in the 1-D integrated slab anomaly rather than a change in the geometry of the slab, the tectonic significance of which is discussed in the following section.

3.2. Sub-Moho Fore-Arc Anomaly

Directly below the fore arc in the mantle and above the slab anomaly, we observe a large negative velocity perturbation anomaly ($< -5\%$) with absolute velocities as low as 3.95 km/s (Figure 6a). In the 80 km depth slice (Figure 5a), the anomaly is bounded by the Slab 1.0 contour extending to just inboard of the active volcanic arc except in the north where it appears to extend well into the back-arc region. In cross section, the sub-Moho fore-arc anomaly has much lower absolute velocities (Figure 6a) and a lower depth limit of about ~60–70 km (Figures 6a–6d) and has a clear separation from the back-arc section of the anomaly (Figure 6a). For this reason, we separate the negative velocity perturbation anomaly into two distinct anomalies and interpret the back-arc section as a separate tectonic feature unrelated to the sub-Moho fore-arc anomaly.

3.3. Sub-Moho Slab Transition Anomaly

The sub-Moho slab transition anomaly appears connected to the elongated sub-Moho fore-arc anomaly at shallow mantle depths (Figure 5a) but is a separate distinct feature by 105 km depth (Figure 5b) completely located in the back arc. In the 105 km depth slice (Figure 5b), the sub-Moho slab transition anomaly is bounded to the west by the Slab 1.0 contour and is a localized feature observed spanning the transition between shallow slab and normal slab geometries. At the 130 km depth slice (Figure 5c), the negative perturbation anomaly (~ -5%) associated with the feature is barely visible, and by the 155 km depth slice (Figure 5d), the anomaly is no longer distinguishable as a separate feature in the mantle. In cross section, the anomaly narrows to the

south (Figure 6c) from its greatest trench-perpendicular extent in the north where it is bounded by the Holocene arc and back-arc volcanism (Figure 6a). As the anomaly narrows to the south, it is observed under slightly higher topography and tends to follow the lateral extent of shallow midcrustal low-velocity zone (Figures 6a–6c). This observational correlation between the along-strike extent of the sub-Moho slab transition anomaly with both slightly elevated topography and a low-velocity zone in the shallow crust appears to be a robust feature as all three observations rapidly terminate south of Lake Titicaca (Figure 6e). For comparison, we have included a 1-D S wave and phase velocity profile from a point located in the center of the anomaly (Figure 4b) where both the shallow crustal low-velocity zone and the upper mantle low-velocity zone (the sub-Moho slab transition anomaly) can be seen in the data (phase velocities). Additionally, the shallow crustal low-velocity zone extends north of the anomaly (Figure 6e) further indicating that both features are not a related inversion artifact (e.g., vertical oscillation from underdamping or overiterating) but a robust feature of the model.

3.4. Sub-Moho Sub-Andean Anomaly

The uppermost mantle below the sub-Andean zone and continuing eastward under the foreland basin is 1–4% slower than our starting model (Figures 6a–6d). This negative velocity anomaly extends as far to the east as we have good resolution and is bounded to the west by the sub-Moho Altiplano anomaly (Figure 5a). The negative velocity perturbation observed below the sub-Andean zone and Chaco foreland basin gradationally increases to a positive perturbation anomaly between 100 and 150 km (Figures 6a–6d). In general, the positive perturbation anomaly mirrors the lateral extent of the sub-Moho negative velocity anomaly except for our southernmost Bolivian cross section (Figure 6d) where the anomaly appears to connect with the sub-Moho Altiplano anomaly. We include both the negative and positive velocity perturbation under the sub-Andean zone and Chaco foreland basin (Figure 4c) when referencing the sub-Moho sub-Andean anomaly in subsequent sections.

3.5. Sub-Moho Altiplano Anomaly

Observed over roughly the same depth ranges as the sub-Moho slab transition anomaly, the sub-Moho Altiplano anomaly is a ~1–4% perturbation anomaly that follows the internally drained portion of the Altiplano at the crust-mantle boundary (Figure 5a). This feature is best expressed at the crust-mantle boundary becoming increasingly more irregular with depth and is nearly indistinguishable as a coherent anomaly by the 130 km depth slice (Figure 5c). In some cross sections, the anomaly is well defined with a clear lateral and vertical boundary (Figures 6a and 6c), and in other cross sections, the anomaly extends both laterally and vertically beyond the resolution limits of the model (Figures 6b and 6d). For simplicity, we include only the shallow (<130 km) part of the anomaly when referencing the sub-Moho Altiplano anomaly in section 4. Again, we have included a 1-D S wave and phase velocity profile from a point located just south of Lake Titicaca where the fast-velocity perturbation in the uppermost mantle is easily seen in the phase velocity data (Figure 4a).

4. Discussion

4.1. Subducted Nazca Slab

The Nazca slab anomaly parallels the Slab 1.0 contours [Hayes *et al.*, 2012] and intermediate seismicity particularly well below 80 km and is unambiguously interpreted as the subducted Nazca plate (Figure 6). Imaging a strong and continuous slab anomaly, a first-order feature expected to be visible in our results, provides an additional metric beyond the formal inversion criteria to qualitatively assess the robustness of our velocity model. That we observe good agreement between our Nazca slab anomaly and independent measures of the slab location (e.g., Slab 1.0 contours and intermediate seismicity) indicates that our starting model appropriately incorporates a priori information (e.g., Moho depth and crustal velocities) to help reduce the nonuniqueness allowed for in the ill-posed surface wave inverse problem [Rawlinson *et al.*, 2014]. This suggests that other upper mantle anomalies observed in our results are as qualitatively robust as the Nazca slab anomaly.

A notable deviation of the Nazca slab anomaly from the Slab 1.0 contours and shallow seismicity is observed at depths shallower than 80 km (Figures 6a–6d). At these depths, the slab anomaly appears to either bend near horizontal (Figures 6b and 6c) or weaken producing a necking feature (Figures 6a and 6d) in the anomaly. It is unlikely that our results are imaging a change in the dip of the subducting slab, as the slab geometry

would require unrealistic deformation of the slab over a relatively short distance to connect at the trench. A more realistic explanation for the observed reduction in velocity is a combination of low-velocity sediments entrained in the subduction channel and low-grade to blueschist facies in the oceanic crust. Although this section of the Andean subduction zone is generally described as starved of sediments, and the subduction as erosive, there is an estimated 0.5 km of sediments in the Peru-Chile Trench [Bangs and Cande, 1997] providing a potential source of sediments to entrain along the subduction channel. A similar low-velocity zone at or near the top of the subducting plate has been imaged in major subduction zones around the world [Bostock, 2013], including the central Andes [Dorbath *et al.*, 2008; Ma and Clayton, 2015], with varying sediment fluxes available in each subduction zone [Rea and Ruff, 1996] suggesting that entrained sediments along the subduction channel alone cannot explain the low-velocity zone we image. Calling on thermal/petrologic models of slab metamorphism, Bostock [2013] interpreted the ubiquitous but variable in downdip extent, upper slab low-velocity zone as marking the transition to eclogite facies in the subducting oceanic crust. Starting at depths of ~ 40 km, eclogitization of the subducting oceanic crust is expected to occur in warm subduction zones, with cold subduction zones delaying the eclogitization depth up to ~ 90 km [Hacker *et al.*, 2003]. We interpret the low-velocity feature in the upper part of the subducting Nazca slab as marking the downdip limit of oceanic crust that has not metamorphosed into eclogite facies. The downdip limit of the low-velocity anomaly (~ 80 km) we see in the subducting slab suggests that this section of the central Andes subduction zone is a cold to intermediate temperature subduction zone and is consistent with other seismic studies [Dorbath *et al.*, 2008; Ma and Clayton, 2015].

4.2. Serpentinized Mantle Fore Arc

Serpentinite in the fore-arc mantle wedge can have significant effects on the distribution of seismicity in a subduction zone and can inform seismic hazard analysis. For example, the downdip rupture limits of large megathrust earthquakes are thought to be controlled by a change in the stress regime along the interface between the subducting slab and the serpentinized mantle effectively decoupling the mantle from the slab [Oleskevich *et al.*, 1999; Wada *et al.*, 2008]. Additionally, buoyancy forces associated with a reduced density in the serpentinized mantle can drive the exhumation of high and ultrahigh pressure rocks [Pilchin, 2005]. Serpentinization of the mantle may have even had significant effects on eustatic sea level changes over the last 600 Myr acting as a mantle water reservoir [Rüpke *et al.*, 2004]. Thus, for many reasons, characterizing both the spatial extent and amount of serpentinization in the mantle fore-arc wedge across our study area is important and warrants a discussion.

The main serpentine group mineral expected to form in the ultramafic mantle fore-arc temperature and pressure conditions is antigorite (HT serpentinite), which is stable between depths of ~ 30 and 150 km and temperatures of 300 and 720°C [Ulmer and Trommsdorff, 1995]. Although antigorite is stable to depths of ~ 150 km, the mantle wedge geothermal gradient confines the stability of antigorite to a narrow channel along the relatively cooler subducting slab concentrating most of the serpentinization in the mantle fore arc at depths shallower than ~ 50 –60 km [Hilairt and Reynard, 2009]. Serpentinization of the mantle fore arc also reduces its *S* wave velocity significantly compared to its peridotitic protolith providing a diagnostic measure of its presence [Bostock *et al.*, 2002]. We observe such a reduced *S* wave velocity structure ($< -5\%$) in the form of a negative velocity perturbation (sub-Moho fore-arc anomaly) in our results. A velocity reduction of greater than 5% cannot be explained by a positive thermal anomaly alone, especially considering the location of the anomaly in the nose of the mantle wedge, which is expected to be cool compared to the adjacent mantle wedge. In our cross sections that show the fore arc (Figures 6a–6d), the anomaly extends to a depth of ~ 60 km, the lower limit of stable antigorite in the mantle wedge. There are also fewer earthquakes along the interface between the slab and the anomalously slow mantle wedge (Figures 6a–6d) consistent with decoupling of a serpentinized mantle along the subduction zone interface. We interpret this low-velocity anomaly as the signature of a serpentinized mantle fore-arc wedge.

A serpentinized mantle wedge composed of pure antigorite (100%) is expected to have an *S* wave velocity of ~ 3.67 km/s [Ji *et al.*, 2013] compared to a ~ 4.45 –4.6 for a peridotite with 0% serpentinization [Christensen, 1966]. Using a linear velocity gradient between 100% antigorite (3.67 km/s) and a peridotite with 0% serpentinization (4.45–4.6 km/s), our lowest velocities in the sub-Moho fore-arc anomaly of 3.95 km/s suggests as much as ~ 65 –70% HT serpentinization in the mantle fore arc. Previous studies in northern Chile (south of our study area) have imaged a similar low-velocity zone in the upper mantle fore

arc suggesting serpentinization as a possible explanation [Graeber and Asch, 1999; Sodoudi et al., 2011]. Our estimate of ~65–70% serpentinization is consistent with other subduction zones [Ji et al., 2013] further supporting a serpentinized mantle fore-arc interpretation of our sub-Moho fore-arc anomaly.

4.3. Focused Slab Dehydration

At the leading edge of the transition between flat and normal subduction is the sub-Moho slab transition anomaly, a low-velocity anomaly as slow as 4.22 km/s (~6%) and much slower than other parts of the model in the same depth range (80–120 km). Here the unique subduction geometry heavily distorts the slab forming a near-90° bend in the slab around 100 km depth (Figure 5b). This anomaly is east of the main volcanic arc but may represent a concentration of fluid coming off the distorted slab. Wagner et al. [2006] observed a similar low *S* wave anomaly at the leading edge of the Pampean flat slab along the Chile/Argentina border. The low *S* wave anomaly (low *P* wave, high *V_p/V_s*) was interpreted by Wagner et al. [2006] as the southward flow of asthenosphere responding to the southward migration of the flat slab. Thus, the leading edge of flat/shallow slabs migrating in a trench-parallel fashion may combine horizontal asthenospheric flow with normal corner flow to produce the anomalously low velocities we image as the sub-Moho slab transition anomaly.

4.4. Brazilian Cratonic Lithosphere?

Along the northern CAP, several studies at different latitudes have argued for the underthrusting of Brazilian cratonic lithosphere beneath the Eastern Cordillera [Dorbath et al., 1993; Lamb et al., 1996; Myers et al., 1998; Beck and Zandt, 2002; Phillips et al., 2012; Ma and Clayton, 2014]. Most studies do not have data coverage east of the Eastern Cordillera and sub-Andean zone making it difficult to image the undeformed Brazilian craton that is coming into the system. Using a dense temporary network (Peru Subduction Experiment, PeruSE) spanning southernmost Peru and a small area of Bolivia north of Lake Titicaca, Phillips et al. [2012] used local tomography and receiver functions to image a midcrustal (~40 km) discontinuity that they interpreted as underthrusting Brazilian shield. In Phillips et al. [2012] interpretation, the underthrusting portion of the Brazilian shield extends beneath the entire Altiplano ending at the Western Cordillera with no corresponding cratonic mantle root. With the same dense PeruSE array, Ma and Clayton [2014] used ambient noise and two-plane wave tomography (similar to the methods used in this study) to image the *S* wave velocity structure below their array. Just north of Lake Titicaca in Bolivia, Ma and Clayton [2014] image a fast-velocity anomaly in the uppermost mantle (60–100 km) that they interpret as the leading edge of the sub-Moho Brazilian shield. Although the lateral and vertical extents of fast-velocity anomalies in these studies vary, they all evoke some underthrusting Brazilian cratonic lithosphere beneath the Eastern Cordillera in their interpretations. We observe some fast-velocity anomalies below the Eastern Cordillera (sub-Moho Altiplano anomaly) but notice a negative velocity anomaly in the uppermost mantle beneath the sub-Andes and Chaco foreland basin (sub-Moho sub-Andean anomaly), which is initially inconsistent with underthrusting of undisrupted Brazilian cratonic lithosphere.

One possible reason for the apparent disagreement between our results and previous studies' interpretations of underthrusting Brazilian cratonic lithosphere may be the limited aperture available to many of the previous studies. A limited aperture is seen in the surface wave tomography of Ma and Clayton [2014] where their stations only extend inboard of the trench to the boundary between the Altiplano and the Eastern Cordillera. This limits their lateral resolution to just north of Lake Titicaca in Bolivia where they image a fast-velocity anomaly in the uppermost mantle (60–100 km) that they interpret as the leading edge of the sub-Moho Brazilian shield. The location of this anomaly corresponds to the northern end of our sub-Moho Altiplano anomaly (Figure 5a). Over roughly the same depth range, Ma and Clayton [2014] observe a low-velocity anomaly that corresponds to the location of our sub-Moho slab transition anomaly further indicating that our results are imaging the same features of the upper mantle. Our larger station aperture allows us to image further east of the high-velocity anomaly interpreted as underthrusting Brazilian cratonic lithosphere by many previous studies where we observe an eastern limit to the high-velocity anomaly that transitions into a slow uppermost mantle anomaly below the sub-Andes (sub-Moho sub-Andean anomaly). We suggest that many of the features interpreted as underthrusting Brazilian shield by previous studies are imaging the eastern extent of our sub-Moho Altiplano anomaly. If this interpretation in the context of previous studies is correct, it fails to explain the absence of Brazilian cratonic lithosphere coming into the fold-and-thrust system where as much as 300 km of upper crustal shortening has been measured and suggests that much of the Brazilian cratonic lithosphere has been removed in the past [McQuarrie et al., 2005].

One possible explanation for the absence of a fast-velocity anomaly beneath the sub-Andes and Chaco foreland basin is that the Brazilian cratonic mantle lithosphere has been removed or disrupted along this section of the Andes. Flat-slab subduction has been postulated to have occurred along nearly the entire South American margin since 40 Ma [Ramos and Folguera, 2009]. The late-Eocene to Oligocene Altiplano flat-slab episode started ~35 Ma lasting approximately 10 Myr under what is now the northern CAP [James and Sacks, 1999] and is one such mechanism capable of removing the cratonic lithosphere. Steepening of the Altiplano flat slab and corresponding expansion of the mantle wedge resulted in an influx of hot asthenosphere producing widespread bimodal volcanism beneath the Altiplano and Eastern Cordillera [Ramos and Folguera, 2009]. Destruction or modification of the cratonic mantle root may have occurred further under the sub-Andes and Chaco foreland basin as a result of the flat-slab hydrating overriding asthenosphere. As the flat slab begins resuming normal subduction, fertile asthenosphere flows in from the east to fill the space created by the steepening slab. This newly hydrated fertile mantle can destroy/modify the existing craton lithosphere through melt-peridotite reactions [Kusky *et al.*, 2014]. The cratonic lithosphere may be heavily altered (metasomatized) without requiring an abundance of surface volcanism through these types of reactions [Foley, 2008]. This is consistent with the low velocities we observe in the uppermost mantle beneath the sub-Andes and Chaco foreland basin (sub-Moho sub-Andean anomaly) being associated with a heavily altered (metasomatized) Brazilian cratonic mantle lithosphere. Additional evidence for the absence of undisrupted cratonic lithosphere is observed in a recent finite frequency teleseismic tomography study where Scire *et al.* [2016] observed slow-velocity perturbations in both P and S wave tomography under (~90 km) the sub-Andes and Chaco foreland basins. Our results cannot uniquely distinguish between a completely absent or a heavily altered (metasomatized) Brazilian cratonic mantle lithosphere beneath the sub-Andes and Chaco foreland basin.

Another possible explanation for the absence of a fast-velocity anomaly beneath the sub-Andes and Chaco foreland basin is seismic anisotropy. In this study we used Rayleigh waves, which are only sensitive to the vertically polarized S wave velocity structure (V_{sv}). Love waves are sensitive to the horizontality polarized S wave velocity structure (V_{sh}), and differences in the S wave velocity structure measured from Love and Rayleigh waves is referred to as radial anisotropy ($V_{sv} \neq V_{sh}$). Lebedev *et al.* [2009] measured surface wave dispersion using both Love and Rayleigh waves across seven different cratonic locations. A consistent observation across the seven cratonic locations was significant radial anisotropy ($V_{sv} < V_{sh}$) in the upper mantle extending to a depth of ~100–150 km. At some locations such as the Parana basin in South America, the vertically polarized S wave velocity structure (Rayleigh waves) is slower than 4.5 km/s in the uppermost mantle. Lebedev *et al.* [2009] interpreted this upper mantle radial anisotropy as horizontal fabrics inherited during the formation of the craton through ductile flow in the cratonic lithosphere. Our sub-Moho sub-Andean anomaly has the same general character (slow uppermost mantle gradually increasing with depth) as the vertically polarized S wave velocity structures imaged below various cratons by Lebedev *et al.* [2009], but potentially more significant is the observation that our upper mantle low-velocity transitions to a fast perturbation anomaly at about the same depth (~100–150 km) as radial anisotropy signatures disappear from the cratonic models.

If the low-velocity uppermost mantle beneath the sub-Andes and Chaco foreland basin (sub-Moho sub-Andean anomaly) is a signature of radial anisotropy, we are imaging the undeformed section of the Brazilian cratonic mantle lithosphere where the original horizontal fabric is still intact. The potential existence of radial anisotropy in the upper mantle beneath the sub-Andes and Chaco foreland basin has important implications for interpreting the nature of the sub-Moho Altiplano anomaly. Since the low-velocity uppermost mantle section of the sub-Moho sub-Andean anomaly abuts the fast velocities of the sub-Moho Altiplano anomaly, it is possible that we are imaging the same tectonic feature (cratonic lithosphere) where the fast velocities observed under the Altiplano are part of the Brazilian shield that has lost its original horizontal fabric. The strong spatial correlation between sub-Moho Altiplano anomaly and the relatively low topography of the Altiplano basin explored in the next section is inconsistent with that interpretation, and we favor a different tectonic explanation for the sub-Moho Altiplano anomaly.

4.5. Mantle Isostatic Contributions to Topography

The sub-Moho Altiplano anomaly (>4.5 km/s) appears to be the northern continuation of a similar upper mantle fast anomaly imaged in a previous regional P wave traveltime tomography study across the southern CAP [Myers *et al.*, 1998]. If this interpretation is correct, a seismically fast upper mantle would underlie nearly

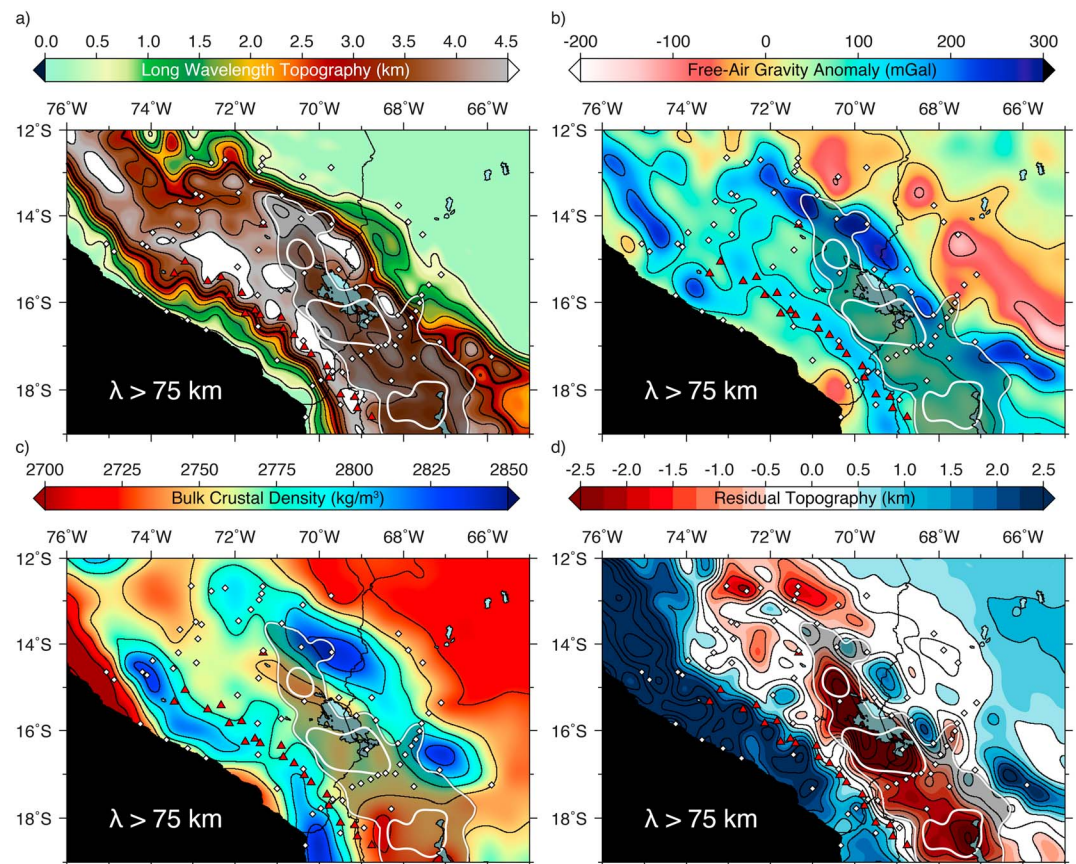


Figure 7. (a) Map of long-wavelength (>75 km) topography, (b) long-wavelength (>75 km) free-air gravity anomaly [Bonvalot *et al.*, 2012], (c) long-wavelength (>75 km) bulk crustal density, and (d) long-wavelength (>75 km) residual topography. The sub-Moho Altiplano anomaly (>4.5 km/s) is contoured by the thin white line with velocities greater than 4.6 km/s shown with thick white lines.

all of the relatively low topography forming the internally drained Altiplano basin. The correlation between the sub-Moho Altiplano anomaly and low topography of the Altiplano is especially striking when compared against the long-wavelength filtered topography (Figure 7a). Of particular interest is the distribution of localized zones of faster material (>4.6 km/s) enclosed by the sub-Moho Altiplano anomaly. We observe three such zones, two located at the north and south ends of Lake Titicaca and one beneath Lake Poopo (Figure 7a). The southernmost zone located beneath Lake Poopo overlaps with the tomography of Myers *et al.* [1998] where they observe a similar zone of localized faster material (up to 10% faster). The location of the sub-Moho Altiplano anomaly beneath the long-wavelength filtered relatively low topography forming the internally drained Altiplano basin and localized zones of even faster material below the modern depositional zones is suggestive of an isostatic relationship between the sub-Moho Altiplano anomaly and the modern surface topography.

A near-zero free-air gravity anomaly (Figure 7b) under the core of the northern CAP [Bonvalot *et al.*, 2012] suggests that the lithosphere is isostatically compensated; however, isostatically compensated lithosphere is dependent on several crustal and mantle properties. Before investigating the potential mantle contributions to the modern surface topography, we first evaluate potential crustal effects (e.g., density differences or thickness variations) capable of producing the relatively low topography of the Altiplano basin by calculating the bulk crustal density structure from our velocity model (Figure 7c). In general, the low topography of Altiplano would predict a thinner and/or denser crust (on long wavelengths) relative to the higher elevations of the Eastern Cordillera or northernmost CAP in southern Peru [Molnar and England, 1990] if the crust is isostatically compensated. However, some of the lowest crustal densities we observe are located under the Altiplano (Figure 7c) along with some of the thickest crust in the area (Figure 2), which is inconsistent with an

isostatically compensated crust. An alternative way to achieve an isostatically compensated lithosphere beneath the Altiplano, consistent with the observed near-zero free-air gravity anomaly, would include the presence of an attached root in the uppermost mantle. A dense mantle root attached to the Altiplano crust would act to suppress the topography beneath the thick and less dense crust of the Altiplano, which would otherwise predict higher elevations for an isostatically compensated crust.

One way to test this explanation is to compare the observed topography (Figure 7a) with the topography predicted from isostatically compensated crust using our crustal thickness and density models. For our purposes, Airy isostatic equilibrium is achieved if

$$h_e \rho_a + h_c \rho_c + h_r \rho_m = h_r \rho_c + h_c \rho_c + h_e \rho_c, \quad (1)$$

where h_r is the height of the crustal root below the reference crustal thickness, h_c is the height of the reference crust, h_e is the height of the crustal elevation above the reference crustal thickness, ρ_m is the density of the mantle, ρ_a is the density of air, and ρ_c is the density of the crust. If we assume that the term with the density of air has a negligible effect, we can rearrange equation (1) to solve for the elevation change above the height of the reference crust given by

$$h_e = \frac{h_r (\rho_m - \rho_c)}{\rho_c}. \quad (2)$$

Since we do not know the height of the root below the reference crust, but we know the height of the reference crust h_c , the height of the elevation above the reference crust h_e , and the total height of the new crust h_t given by

$$h_t = h_r + h_c + h_e, \quad (3)$$

we can solve for the height of the root below the reference crust by rearranging equation (3) as

$$h_r = h_t - h_c - h_e. \quad (4)$$

Substituting equation (4) into equation (2), we arrive at an expression for the predicted elevation h_e that can be rewritten as

$$h_e = \frac{h_t - h_c}{1 + \left(\frac{\rho_c}{\rho_m - \rho_c} \right)}, \quad (5)$$

where the predicted elevation h_e is now a function of three terms we can measure (crustal thickness, uppermost mantle density, and crustal density) and one we have to assume (reference crustal height). For each 1-D location in our model, we calculate the predicted elevation and subtract it from the observed elevation to determine the residual topography using a reference crustal height of 40 km (Figure 7d). If we use a 35 km reference crustal height or a constant density contrast between the crust and mantle, we observe a similar spatial correlation between areas where elevations are lower than the crustal thickness/density would predict and the sub-Moho Altiplano anomaly.

Our residual topography map is only a first-order approximation and not equally valid in all areas, as our model does not account for flexural support or the possible effects of dynamic topography. For example, areas in the fore arc or Eastern Cordillera with positive residual topography likely have some component of elastically supported topography. Additionally, the high-amplitude long-wavelength free-air gravity anomaly along the Eastern Cordillera (Figure 7b) suggests that the lithosphere is not isostatically compensated, and therefore, we would not expect good agreement between the predicted elevations and observed topography (e.g., large residual topography anomaly). Although dynamic topography driven mainly by the subducting Nazca plate is not accounted for in our simple Airy isostatic approach, the modeled wavelength of slab-induced dynamic topography [Shephard *et al.*, 2010; Dávila and Lithgow-Bertelloni, 2013] is considerably longer than the wavelengths of residual topography presented here (Figure 7d) and is an insufficient explanation for the low topography of the Altiplano. If the sub-Moho Altiplano anomaly was simply an area of normal or slightly faster (and by proxy denser) ambient mantle, the larger density contrast between the mantle and crust would predict higher elevations for a similar crustal thickness of equal or greater density than areas where the sub-Moho Altiplano anomaly is absent. In the absence of this observation, we interpret the sub-Moho Altiplano anomaly beneath the Altiplano basin as an upper mantle

lithospheric root that is isostatically depressing the current topography of the northern CAP. The tectonic source of this attached root in the uppermost mantle beneath the Altiplano is explored in the following section.

4.6. Lithospheric Delamination as an Uplift Mechanism

Lithospheric delamination has been long postulated as a contributing mechanism to the growth of the central Andes [Kay and Kay, 1993; Kay et al., 1994; Beck and Zandt, 2002; McQuarrie et al., 2005; Asch et al., 2006; Garzzone et al., 2006; Ghosh et al., 2006; DeCelles et al., 2009], but only recently has the data coverage and methodology become available to investigate the structure of the uppermost mantle in sufficient detail [e.g., Calixto et al., 2013; Beck et al., 2015; Scire et al., 2016]. Although seismic models of the uppermost mantle alone cannot determine the timing and evolution of delamination events, they are particularly useful in discriminating against different models and stages of lithospheric delamination. Our results are not particularly sensitive to smaller, kilometer scale “drips” [e.g., Murray et al., 2015] but should be able to resolve larger-scale delamination of the lithosphere, especially if the delamination affects the thermal profile of the uppermost mantle [Sobolev and Babeyko, 2005; Babeyko et al., 2006; Sobolev et al., 2006; Krystopowicz and Currie, 2013]. The coupled, thermomechanical, numerical modeling of Sobolev et al. [2006] was intended to investigate the dynamic interaction of the subducting and overriding plates (e.g., absolute plate motions and plate interface shear coupling) and initial lithospheric structure (e.g., crustal thickness) on the intensity of tectonic shortening, but their model also makes specific predictions about density, temperature, and structural variations in the crust and uppermost mantle that to first order, our *S* wave velocity model is capable of imaging by proxy. We therefore compare our cross-section results (Figure 6) with the numerical modeling of Sobolev et al. [2006] and observe general agreement between modeled sub-Moho lithospheric structures and our *S* wave velocity model.

Of particular interest is the agreement of our sub-Moho Altiplano anomaly and western extent of our sub-Moho sub-Andean anomaly with a foreland dipping thermal aureole in the upper mantle associated with delaminating lithosphere (Figures 6b and 6d). In the numerical model, the foreland dipping upper mantle thermal feature connects to the crust/lithosphere below the location equivalent to the Eastern Cordillera continuing west under the Altiplano and is juxtaposed to the east by cratonic lithosphere. The upper mantle thermal feature results from lower crust eclogitization mineral reactions that increase the bulk density of the lower crust to values greater than mantle peridotite, resulting in foundering of the lithosphere that extends to a depth of nearly 300 km. This continuous (base of crust to ~300 km) density/compositional feature is much thinner than its thermal expression, and if delaminating lithosphere is a correct interpretation of the sub-Moho Altiplano anomaly, our *S* wave velocity results are likely imaging a thermal component of the foundering root as well. In a recent finite frequency tomography study that included *P* and *S* waves, Scire et al. [2016] imaged a similar positive *S* wave velocity perturbation roughly coincident with our sub-Moho Altiplano anomaly in the uppermost mantle (<120 km) with a localized positive anomaly beneath the sub-Andes extending to a depth of ~300 km and suggested that this anomaly may be delaminated lithosphere. Scire et al. [2016] lacked the resolution in the uppermost mantle to establish if the positive velocity anomaly was connected to the base of the crust or if it exists as a separate mantle anomaly. If the *P* wave tomography anomaly is the deeper expression of the sub-Moho Altiplano anomaly, our results suggest that the anomaly is a continuous vertical feature (laterally localized, Figures 6b and 6d) extending from the base of crust to as deep as 300 km.

The correlation between the sub-Moho Altiplano anomaly and low topography of the Altiplano basin suggests a strong isostatic relationship between the sub-Moho Altiplano anomaly and modern surface topography. Additionally, the agreement between our upper mantle results, recent finite frequency tomography results [Scire et al., 2016], and coupled, thermomechanical, numerical modeling of lithospheric delamination [Sobolev et al., 2006] is consistent with the sub-Moho Altiplano anomaly representing a dense piece of lithosphere in the process of delaminating. We prefer this interpretation of the anomaly but acknowledge that it is a nonunique interpretation. An alternative interpretation of the sub-Moho Altiplano anomaly is that it represents the leading edge of the underthrusting Brazilian cratonic lithosphere. In this interpretation, the leading edge of the underthrusting Brazilian cratonic lithosphere has lost its initial horizontal fabric and is no longer radially anisotropic resulting in our *S* wave velocity model imaging it as a fast upper mantle anomaly below the Altiplano and Eastern Cordillera.

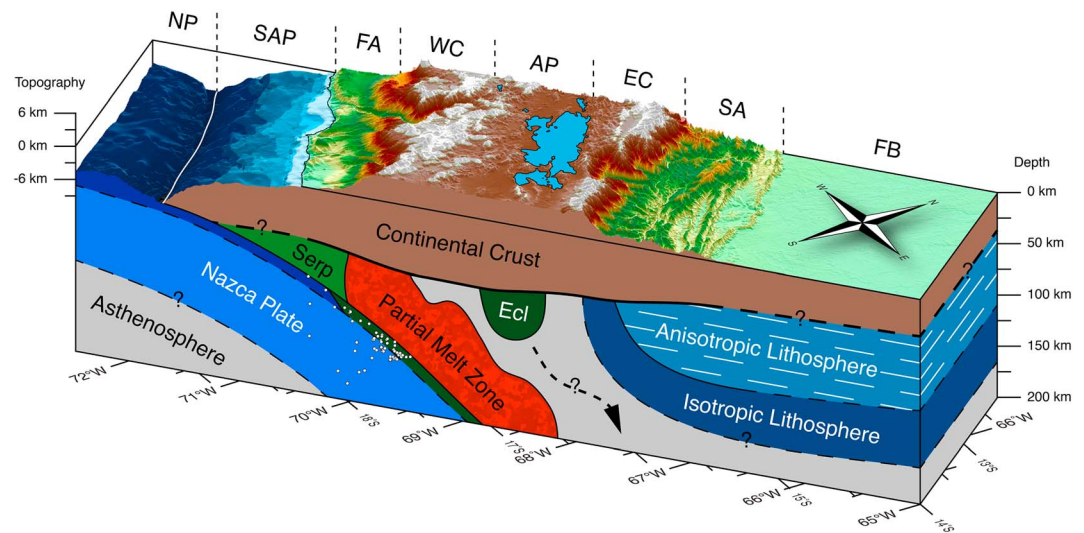


Figure 8. Conceptual summary figure showing our preferred interpretation of mantle anomalies discussed in the main text. Cross-section face is approximately the 2-D cross section shown in Figure 6d. NP, Nazca Plate; SAP, South America Plate; FA, fore arc; WC, Western Cordillera; AP, Altiplano; EC, Eastern Cordillera; SA, sub-Andes; FB, foreland basin; Serp, serpentinized mantle fore arc; Ecl, cold and/or lower crustal eclogitization.

5. Conclusions

In this surface wave tomography study, we integrated dispersion data (8–50 s) from a previous ambient noise tomography study [Ward *et al.*, 2013, 2014b] with longer period (25–143 s) dispersion data measured using the two-plane wave tomography method [Forsyth *et al.*, 1998; Forsyth and Li, 2005]. We inverted the surface wave dispersion data for an *S* wave velocity model using all appropriate a priori information (e.g., crustal velocities and crustal thickness models). The five main features of our *S* wave velocity model and preferred interpretations summarized in Figure 8 are the following:

1. There is a high-velocity slab with a shallow (<80 km) low velocity in the upper part of the slab that is no longer visible at depths greater than ~80 km. Calling on thermal/petrologic models of slab metamorphism, Bostock [2013] interpreted the ubiquitous but variable in downdip extent, upper slab low-velocity zone seen in major subduction zones around the globe as marking the transition to eclogite facies in the subducting oceanic crust at ~45 km in “warm” subduction zones and up to 80–120 km depth for “cold” subduction zones. We interpret the low-velocity feature in the upper part of the subducting Nazca slab as marking the downdip limit of oceanic crust that has not metamorphosed into eclogite facies. The downdip limit of the ~80 km low-velocity anomaly we see in the subducting slab suggests that this section of the central Andes subduction zone is a “cold” or “intermediate” temperature subduction zone.
2. There is a large negative velocity perturbation (< –5%) with absolute velocities as low as 3.95 km/s directly below the fore arc in the mantle above the slab. Serpentinization of the mantle fore arc reduces its *S* wave velocity significantly compared to its peridotitic protolith providing a diagnostic measure of its presence [Bostock *et al.*, 2002]. We observe such a reduced *S* wave velocity structure (< –5%) in the form of a negative velocity perturbation below the fore arc in our results. A velocity reduction of greater than 5% cannot be explained by a positive thermal anomaly alone, especially considering the location of the anomaly in the nose of the mantle wedge, which is expected to be cool compared to the adjacent mantle wedge. Our absolute velocity of ~3.95 km/s in the fore-arc mantle suggests ~65–70% serpentinization and is consistent with other subduction zones supporting a serpentinized mantle fore-arc interpretation.
3. There is a low-velocity anomaly in the back arc above the slab where the slab geometry transitions from near horizontal to a normal dip. The low velocity we observe in the back arc where the slab transitions between flat and normal subduction is as low as 4.22 km/s (~6%) and much slower than other parts of the model in the same depth range (80–120 km). Given the distribution of seismicity below the back-arc low-velocity zone, occurring at depths associated with dehydration reactions in the subducting slab [Schmidt and Poli, 1998], and the unique slab geometry where the slab forms a near-90° bend, we interpret the velocity anomaly as a region in the upper mantle with concentrated levels of partial melt (~1%).

4. There is a negative velocity anomaly extending as far to the east as we have good resolution below the sub-Andean zone and Chaco foreland basin gradually increasing to a positive perturbation anomaly between 100 and 150 km. One possible explanation for the absence of a fast-velocity anomaly beneath the sub-Andes and Chaco foreland basin is that the Brazilian cratonic mantle lithosphere has been removed or disrupted along this section of the Andes [O'Driscoll *et al.*, 2012]. Another possible explanation for the absence of a fast-velocity anomaly beneath the sub-Andes and Chaco foreland basin is seismic anisotropy. In this study we used Rayleigh waves, which are only sensitive to the vertically polarized S wave velocity structure (V_{sv}). Lebedev *et al.* [2009] measured surface wave dispersion using both Love and Rayleigh waves across seven different cratonic locations. A consistent observation across the seven cratonic locations was significant radial anisotropy ($V_{sv} < V_{sh}$) in the upper mantle extending to a depth of ~ 100 – 150 km. If the low-velocity uppermost mantle beneath the sub-Andes and Chaco foreland is a signature of radial anisotropy, we are imaging the undeformed section of the Brazilian cratonic mantle lithosphere where the original horizontal fabric is still intact.
5. There is a high-velocity feature in the mantle above the slab that extends along the length of the Altiplano from the base of the Moho to a depth of ~ 120 km with the highest velocities observed under Lake Titicaca and Lake Poopo. The fast Altiplano anomaly is a ~ 1 – 4% perturbation anomaly that follows the internally drained portion of the Altiplano at the crust-mantle boundary. The correlation between the sub-Moho Altiplano anomaly and low topography of the Altiplano basin suggests a strong isostatic relationship between the sub-Moho Altiplano anomaly and modern surface topography. Additionally, the agreement between our upper mantle results; recent finite frequency tomography results [Scire *et al.*, 2016]; and coupled, thermomechanical, numerical modeling of lithospheric delamination [Sobolev *et al.*, 2006] is consistent with the sub-Moho Altiplano anomaly representing a dense piece of lithosphere in the process of delaminating. Determining if the high-velocity feature represents a small lithospheric root or a delaminating lithospheric root extending ~ 300 km into the mantle requires more integration of observations, but either interpretation shows a strong geodynamic connection with the uppermost mantle and the current topography of the northern CAP.

Acknowledgments

This work was funded in part by NSF grants EAR-1415914, EAR-0943991, and EAR-0907880. The facilities of the IRIS Data Management System, and specifically the IRIS Data Management Center, were used for access to waveform and metadata required in this study. The IRIS DMS is funded through the National Science Foundation and specifically the GEO Directorate through the Instrumentation and Facilities Program of the National Science Foundation under Cooperative Agreement EAR-1063471. The Global Seismographic Network (GSN) is a cooperative scientific facility operated jointly by the Incorporated Research Institutions for Seismology (IRIS), the United States Geological Survey (USGS), and the National Science Foundation (NSF). We acknowledge the GEOFON Program of GFZ Potsdam as an additional source of waveform data. Data used in this study can be found at the IRIS Data Management System (<http://ds.iris.edu/ds/nodes/dmc/data/>) and at the GFZ Seismological Data Archive (<http://geofon.gfz-potsdam.de/waveform/>). Initial processing of waveforms was handled using the Seismic Analysis Code (SAC) software [Goldstein *et al.*, 2003; Goldstein and Snoke, 2005], and figures were plotted using the Generic Mapping Tool (GMT) software [Wessel *et al.*, 2013]. We also acknowledge the thoughtful comments from Don Forsyth and one anonymous reviewer. Finally, we thank Estela Minaya and the entire staff of the San Calixto Observatory in La Paz, Bolivia, for their invaluable long-term assistance with our seismic deployments in southern Bolivia as well as Sanja Knezevic Antonijevic for assistance with the TPWT method.

References

- Albuquerque Seismological Laboratory (ASL)/USGS (1993), Global Telemetered Seismograph Network (USAF/USGS), International Federation of Digital Seismograph Networks. Other/Seismic Network, doi:10.7914/SN/GT.
- Allmendinger, R. W., T. E. Jordan, S. M. Kay, and B. L. Isacks (1997), The evolution of the Altiplano-Puna plateau of the central Andes, *Annu. Rev. Earth Planet. Sci.*, *25*, 139–174.
- Antonijevic, S. K., L. S. Wagner, A. Kumar, S. L. Beck, M. D. Long, G. Zandt, H. Tavera, and C. Condori (2015), The role of ridges in the formation and longevity of flat slabs, *Nature*, *524*(7564), 212–215, doi:10.1038/nature14648.
- Armijo, R., R. Lacassin, A. Coudurier-Curveur, and D. Carrizo (2015), Coupled tectonic evolution of Andean orogeny and global climate, *Earth Sci. Rev.*, *143*, 1–35.
- Asch, G., *et al.* (2006), Seismological studies of the central and southern Andes, in *The Andes*, pp. 443–457, Springer, Berlin Heidelberg.
- Babeyko, A. Y., S. Sobolev, T. Vietor, O. Oncken, and R. Trumbull (2006), Numerical study of weakening processes in the central Andean back-arc, in *The Andes, Front. Earth Sci.*, pp. 495–512, Springer, Berlin Heidelberg.
- Baby, P., I. Moretti, B. Guillier, R. Limachi, E. Mendez, J. Oller, and M. Specht (1995), Petroleum system of the northern and central Bolivian sub-Andean zone, in *Petroleum Basins of South America, Memoir*, vol. 62, edited by A. J. Tankard, R. Suárez, and H. J. Welsink, pp. 445–458, AAPG, Bolivia.
- Baby, P., P. Rochat, G. Mascle, and G. Herail (1997), Neogene shortening contribution to crustal thickening in the back arc of the central Andes, *Geology*, *25*(10), 883–886.
- Bangs, N. L., and S. C. Cande (1997), Episodic development of a convergent margin inferred from structures and processes along the southern Chile margin, *Tectonics*, *16*, 489–503, doi:10.1029/97TC00494.
- Barazangi, M., and B. L. Isacks (1976), Spatial distribution of earthquakes and subduction of the Nazca plate beneath South America, *Geology*, *4*, 686–692, doi:10.1130/0091-7613(1976)4.
- Barmin, M. P., M. H. Ritzwoller, and A. L. Levshin (2001), A fast and reliable method for surface-wave tomography, *Pure Appl. Geophys.*, *158*(8), 1351–1375.
- Barnes, J. B., and T. A. Ehlers (2009), End member models for Andean Plateau uplift, *Earth Sci. Rev.*, *97*, 105–132, doi:10.1016/j.earscirev.2009.08.003.
- Baumont, D., A. Paul, S. Beck, and G. Zandt (1999), Strong crustal heterogeneity in the Bolivian Altiplano as suggested by attenuation of L_g waves, *J. Geophys. Res.*, *104*, 20,287–20,305, doi:10.1029/1999JB900160.
- Beck, S., and G. Zandt (2002), The nature of orogenic crust in the central Andes, *J. Geophys. Res.*, *107*(B10), 2230, doi:10.1029/2000JB000124.
- Beck, S. L., G. Zandt, K. M. Ward, and A. Scire (2015), Multiple styles and scales of lithospheric foundering beneath the Puna Plateau, central Andes, in *Geodynamics of a Cordilleran Orogenic System: The Central Andes of Argentina and Northern Chile, Memoir*, vol. 212, edited by DeCelles, P. G., *et al.*, pp. 43–60, Geol. Soc., America, doi:10.1130/2015.1212(03).
- Beck, S., G. Zandt, and L. Wagner (2010), Central Andean uplift and the geodynamics of the high topography, International Federation of Digital Seismograph Networks. Other/Seismic Network, doi:10.7914/SN/ZG_2010.
- Bensen, G. D., M. H. Ritzwoller, M. P. Barmin, A. L. Levshin, F. Lin, M. P. Moschetti, N. M. Shapiro, and Y. Yang (2007), Processing seismic ambient noise data to obtain reliable broad-band surface wave dispersion measurements, *Geophys. J. Int.*, *169*(3), 1239–1260.

- Bensen, G. D., M. H. Ritzwoller, and N. M. Shapiro (2008), Broadband ambient noise surface wave tomography across the United States, *J. Geophys. Res.*, *113*, B05306, doi:10.1029/2007JB005248.
- Bonvalot, S., G. Balmino, A. Briais, M. Kuhn, A. Peyrefitte, and N. Vales (2012), World gravity map, Bureau Gravimetric International (BGI) (CGMW-BGI-CNES-IRD, Paris).
- Bostock, M. G. (2013), The Moho in subduction zones, *Tectonophysics*, *609*, 547–557.
- Bostock, M. G., R. D. Hyndman, S. Rondenay, and S. M. Peacock (2002), An inverted continental Moho and serpentinization of the forearc mantle, *Nature*, *417*, 536–539.
- Brocher, T. M. (2005), Empirical relations between elastic wavespeeds and density in the Earth's crust, *Bull. Seismol. Soc. Am.*, *95*, 2081–2092.
- Cahill, T., and B. L. Isacks (1992), Seismicity and shape of the subducted Nazca Plate, *J. Geophys. Res.*, *97*, 17,503–17,529, doi:10.1029/92JB00493.
- Calixto, F. J., E. Sandvol, S. Kay, P. Mulcahy, B. Heit, X. Yuan, B. Coira, D. Comte, and P. Alvarado (2013), Velocity structure beneath the southern Puna plateau: Evidence for delamination, *Geochem. Geophys. Geosyst.*, *14*, 4292–4305, doi:10.1002/ggge.20266.
- Christensen, N. I. (1966), Elasticity of ultrabasic rocks, *J. Geophys. Res.*, *71*, 5921–5931, doi:10.1029/JZ071i024p05921.
- Davidson, J. P., and S. L. de Silva (1992), Volcanic rocks from the Bolivian Altiplano: Insights into crustal structure, contamination, and magma genesis in the central Andes, *Geology*, *20*, 1127–1130.
- Dávila, F. M., and C. Lithgow-Bertelloni (2013), Dynamic topography in South America, *J. South Am. Earth Sci.*, *43*, 127–144.
- de Silva, S. L. (1989), Altiplano-Puna volcanic complex of the central Andes, *Geology*, *17*, 1102–1106, doi:10.1130/0091-7613(1989)017<1102:APVCOT>2.3.CO;2.
- DeCelles, P. G., M. N. Ducea, P. Kapp, and G. Zandt (2009), Cyclicity in Cordilleran orogenic systems, *Nat. Geosci.*, *2*, 251–257, doi:10.1038/ngeo469.
- Delph, J. R., C. B. Biryol, S. L. Beck, G. Zandt, and K. M. Ward (2015), Shear wave velocity structure of the Anatolian Plate: Anomalous slow crust in southwestern Turkey, *Geophys. J. Int.*, *202*, 261–276, doi:10.1093/gjiras/ggv141.
- Dorbath, C., M. Granet, G. Poupinet, and C. Martinez (1993), A teleseismic study of the Altiplano and the Eastern Cordillera in northern Bolivia: New constraints on a lithospheric model, *J. Geophys. Res.*, *98*, 9825–9844, doi:10.1029/92JB02406.
- Dorbath, C., M. Gerbault, G. Carlier, and M. Guiraud (2008), Double seismic zone of the Nazca plate in northern Chile: High-resolution velocity structure, petrological implications, and thermomechanical modeling, *Geochem. Geophys. Geosyst.*, *9*, Q07006, doi:10.1029/2008GC002020.
- Eakin, C. M., M. D. Long, S. L. Beck, L. S. Wagner, H. Tavera, and C. Condori (2014), Response of the mantle to flat slab evolution: Insights from local S splitting beneath Peru, *Geophys. Res. Lett.*, *41*, 3438–3446, doi:10.1002/2014GL059943.
- Elger, K., O. Oncken, and J. Glodny (2005), Plateau-style accumulation of deformation: Southern Altiplano, *Tectonics*, *24*, TC4020, doi:10.1029/2004TC001675.
- Foley, S. F. (2008), Rejuvenation and erosion of the cratonic lithosphere, *Nat. Geosci.*, *1*, 503–510.
- Forsyth, D. W., and A. Li (2005), Array analysis of two-dimensional variations in surface wave phase velocity and azimuthal anisotropy in the presence of multipathing interference, in *Seismic Earth: Array Analysis of Broadband Seismograms*, *Geophys. Monogr. Ser.*, vol. 157, pp. 81–97, AGU, Washington, D. C.
- Forsyth, D., S. Webb, L. Dorman, and Y. Shen (1998), Phase velocities of Rayleigh waves in the MELT experiment on the East Pacific Rise, *Science*, *280*, 1235–1238, doi:10.1126/science.280.5367.1235.
- Francis, P. W., and S. L. de Silva (1989), Application of the Landsat thematic mapper to the identification of potentially active volcanoes in the central Andes, *Remote Sens. Environ.*, *28*, 245–255.
- Garzzone, C. N., P. Molnar, J. C. Libarkin, and B. J. MacFadden (2006), Rapid late Miocene rise of the Bolivian Altiplano: Evidence for removal of mantle lithosphere, *Earth Planet. Sci. Lett.*, *241*, 543–556.
- Garzzone, C. N., G. D. Hoke, J. C. Libarkin, S. Withers, B. MacFadden, J. Eiler, P. Ghosh, and A. Mulch (2008), Rise of the Andes, *Science*, *320*, 1304–1307, doi:10.1126/science.1148615.
- GFZ German Research Centre for Geosciences and Institut des Sciences de l'Univers-Centre National de la Recherche CNRS-INSU (2006), IPOC Seismic Network. Integrated Plate Boundary Observatory Chile-IPOC, Other/Seismic Network, doi:10.14470/PK615318.
- Ghosh, P., C. N. Garzzone, and J. M. Eiler (2006), Rapid uplift of the Altiplano revealed through ¹³C-¹⁸O bonds in paleosol carbonates, *Science*, *311*, 511–515, doi:10.1126/science.1119365.
- Gilbert, H., Y. Yang, D. W. Forsyth, C. Jones, T. Owens, G. Zandt, and J. Stachnik (2012), Imaging lithospheric foundering in the structure of the Sierra Nevada, *Geosphere*, *8*, 1310–1330, doi:10.1130/GES00790.1.
- Goldstein, P., and A. Snoko (2005), Sac availability for the iris community, DMS Electronic Newsletter VII. 1. [Available at <http://www.iris.edu/news/newsletter/vol7no1/page1.htm>.]
- Goldstein, P., D. Dodge, M. Firpo, and L. Minner (2003), SAC2000: Signal processing and analysis tools for seismologists and engineers, in *Invited Contribution to the IASPEI International Handbook of Earthquake and Engineering Seismology*, edited by W. H. K. Lee et al., pp. 1000, Academic Press, London.
- Graeber, F. M., and G. Asch (1999), Three-dimensional models of P wave velocity and P-to-S velocity ratio in the southern central Andes by simultaneous inversion of local earthquake data, *J. Geophys. Res.*, *104*, 20,237–20,256, doi:10.1029/1999JB900037.
- Hacker, B. R., S. M. Peacock, G. A. Abers, and S. D. Holloway (2003), Subduction factory—2. Are intermediate-depth earthquakes in subducting slabs linked to metamorphic dehydration reactions?, *J. Geophys. Res.*, *108*(B1), 2030, doi:10.1029/2001JB001129.
- Hayes, G. P., D. J. Wald, and R. L. Johnson (2012), Slab1.0: A three-dimensional model of global subduction zone geometries, *J. Geophys. Res.*, *117*, B01302, doi:10.1029/2011JB008524.
- Herrmann, R. B., and C. J. Ammon (2004), Herrmann: Computer programs in seismology-surface waves, receiver functions and crustal structure. Saint Louis University. [Available at <http://www.eas.slu.edu/People/RBHerrmann/ComputerPrograms.html>.]
- Hilaitre, N., and B. Reynard (2009), Stability and dynamics of serpentinite layer in subduction zone, *Tectonophysics*, *465*, 24–29, doi:10.1016/j.tecto.2008.10.005.
- Husson, L. T., and T. Sempere (2003), Thickening the Altiplano crust by gravity-driven crustal channel flow, *Geophys. Res. Lett.*, *30*(5), 1243, doi:10.1029/2002GL016877.
- James, D. E. (1971), Plate tectonic model for the evolution of the central Andes, *Geol. Soc. Am. Bull.*, *82*, 3325–3346, doi:10.1130/00167606(1971)82(3325:PTMFTE)2.0.CO;2.
- James, D. E., and J. W. Sacks (1999), Cenozoic formation of the central Andes: A geophysical perspective, in *Geology and Ore Deposits of the Central Andes*, *Soc. Econ. Geol. Spec. Publ.*, vol. 7, edited by B. Skinner, pp. 1–25, Soc. of Econ. Geol., Littleton, Colo.
- Ji, S., A. W. Li, Q. Wang, C. X. Long, H. C. Wang, D. Marcotte, and M. Salisbury (2013), Seismic velocities, anisotropy, and shear-wave splitting of antigorite serpentinites and tectonic implications for subduction zones, *J. Geophys. Res. Solid Earth*, *118*, 1015–1037, doi:10.1002/jgrb.50110.

- Jordan, T. E., B. L. Isacks, R. W. Allmendinger, J. A. Brewer, A. Ramos, and C. J. Ando (1983), Andean tectonics related to geometry of subducted Nazca plate Andean tectonics related to geometry of subducted Nazca plate, *Geol. Soc. Am. Bull.*, *94*, 341–361.
- Jordan, T. E., J. H. Reynolds III, and J. P. Erikson (1997), Variability in age of initial shortening and uplift in the central Andes, 16–33°S, in *Tectonic Uplift and Climate Change*, edited by W. F. Ruddiman, pp. 41–61, Plenum Press, New York.
- Kay, R. W., and S. M. Kay (1993), Delamination and delamination magmatism, *Tectonophysics*, *29*, 177–189.
- Kay, S. M., B. Coira, and J. Viramonte (1994), Young mafic back arc volcanic rocks as indicators of continental lithospheric delamination beneath the Argentine Puna plateau, central Andes, *J. Geophys. Res.*, *99*, 24,323–24,339, doi:10.1029/94JB00896.
- Kendrick, E., M. Bevis, R. Smalley, B. Brooks, R. Vargas, E. Lauriia, and L. Fortes (2003), The Nazca South America Euler vector and its rate of change, *J. South Am. Earth Sci.*, *16*(2), 125–131, doi:10.1016/S0895-9811(03)00028-2.
- Kennett, B. L. N., E. R. Engdahl, and R. Buland (1995), Constraints on seismic velocities in the Earth from traveltimes, *Geophys. J. Int.*, *122*(1), 108–124.
- Kley, J. (1999), Geologic and geometric constraints on a kinematic model of the Bolivian orocline, *J. South Am. Earth Sci.*, *12*(2), 221–235.
- Krystopowicz, N. J., and C. A. Currie (2013), Crustal eclogitization and lithosphere delamination in orogens, *Earth Planet. Sci. Lett.*, *361*, 195–207, doi:10.1016/j.epsl.2012.09.056.
- Kumar, A., L. S. Wagner, S. L. Beck, M. D. Long, G. Zandt, B. Young, H. Tavera, and E. Minaya (2016), Seismicity and state of stress in the central and southern Peruvian flat slab, *Earth Planet. Sci. Lett.*, *441*, 71–80, doi:10.1016/j.epsl.2016.02.023.
- Kusky, T. M., B. F. Windley, L. Wang, Z. S. Wang, X. Y. Li, and P. M. Zhu (2014), Flat slab subduction, trench suction, and craton destruction: Comparison of the North China, Wyoming, and Brazilian cratons, *Tectonophysics*, *630*, 208–221.
- Lamb, S. (2011), Did shortening in thick crust cause rapid Late Cenozoic uplift in the northern Bolivian Andes?, *J. Geol. Soc.*, *168*(5), 1079–1092, doi:10.1144/0016-76492011-008.
- Lamb, S. (2015), Cenozoic uplift of the central Andes in northern Chile and Bolivia—Reconciling paleoaltimetry with the geological evolution 1, *Canadian J. Earth Sci.*, *53*(999), 1–19.
- Lamb, S., L. Hoke, L. Kennan, and J. Dewey (1996), Cenozoic evolution of the central Andes in Bolivia and northern Chile, in *Orogeny Through Time*, edited by J. P. Burg and M. Ford, pp. 237–264, The Geol. Soc., London.
- Lebedev, S., J. Boonen, and J. Trampert (2009), Seismic structure of Precambrian lithosphere: New constraints from broad-band surface-wave dispersion, *Lithos*, *109*, 96–111.
- Lin, F., M. H. Ritzwoller, J. Townend, S. Bannister, and M. K. Savage (2007), Ambient noise Rayleigh wave tomography of New Zealand, *Geophys. J. Int.*, *170*(2), 649–666.
- Liu, Q., R. D. van der Hilst, Y. Li, H. Yao, J. Chen, B. Guo, S. Qi, J. Wang, H. Huang, and S. Li (2014), Eastward expansion of the Tibetan Plateau by crustal flow and strain partitioning across faults, *Nat. Geosci.*, *7*(5), 361–365.
- Ludwig, W. J., J. E. Nafe, and C. L. Drake (1970), Seismic refraction, in *The Sea*, vol. 4, edited by A. E. Maxwell, pp. 53–84, Interscience, New York.
- Ma, Y., and R. Clayton (2014), The crust and uppermost mantle structure of Southern Peru from ambient noise and earthquake surface wave analysis, *Earth Planet. Sci. Lett.*, *395*, 61–70.
- Ma, Y., and R. W. Clayton (2015), Flat slab deformation caused by interpolate suction force, *Geophys. Res. Lett.*, *42*, 7064–7072, doi:10.1002/2015GL065195.
- McQuarrie, N., B. K. Horton, G. Zandt, S. Beck, and P. G. DeCelles (2005), Lithospheric evolution of the Andean fold-thrust belt, Bolivia, and the origin of the Central Andean Plateau, *Tectonophysics*, *399*, 15–37, doi:10.1016/j.tecto.2004.12.013.
- Molnar, P., and P. England (1990), Late Cenozoic uplift of mountain ranges and global climate change: Chicken or egg?, *Nature*, *346*, 29–34.
- Murray, K. E., Ducea, M. N., and Schoenbohm, L. M. (2015), Foundering-driven lithospheric melting: The source of central Andean mafic lavas on the Puna Plateau (22°S–27°S), in *Geodynamics of a Cordilleran Orogenic System: The Central Andes of Argentina and Northern Chile*, *Memoir*, vol. 212, edited by DeCelles, P. G., et al., pp. 139–166, Geol. Soc., America, doi:10.1130/2015.1212(08).
- Myers, S., S. Beck, G. Zandt, and T. Wallace (1998), Lithospheric-scale structure across the Bolivian Andes from tomographic images of velocity and attenuation for P and S waves, *J. Geophys. Res.*, *103*, 21,233–21,252, doi:10.1029/98JB00956.
- Norabuena, E., L. Leffler-Griffin, A. Mao, T. Dixon, S. Stein, I. S. Sacks, L. Ocala, and M. Ellis (1998), Space geodetic observation of Nazca-South America convergence along the central Andes, *Science*, *279*, 358–362, doi:10.1126/science.279.5349.358.
- O'Driscoll, L. J., M. A. Richards, and E. D. Humphreys (2012), Nazca-South America interactions and the late Eocene-late Oligocene flat-slab episode in the central Andes, *Tectonics*, *31*, TC2013, doi:10.1029/2011TC003036.
- Oleskevich, D. A., R. D. Hyndman, and K. Wang (1999), The updip and downdip limits to great subduction earthquakes: Thermal and structural models of Cascadia, south Alaska, SW Japan, and Chile, *J. Geophys. Res.*, *104*, 14,965–14,991, doi:10.1029/1999JB900060.
- Phillips, K., R. W. Clayton, P. Davis, H. Tavera, R. Guy, S. Skinner, I. Stubbailo, L. Audin, and V. Aguiar (2012), Structure of the subduction system in southern Peru from seismic array data, *J. Geophys. Res.*, *117*, B11306, doi:10.1029/2012JB009540.
- Pilchin, A. (2005), The role of serpentinization in exhumation of high-to ultra-high pressure metamorphic rocks, *Earth Planet. Sci. Lett.*, *237*, 815–828.
- Porter, R., H. Gilbert, G. Zandt, S. Beck, L. Warren, J. Calkins, P. Alvarado, and M. Anderson (2012), Shear wave velocities in the Pampean flat-slab region from Rayleigh wave tomography: Implications for slab and upper mantle dehydration, *J. Geophys. Res.*, *117*, B11301, doi:10.1029/2012JB009350.
- Ramos, V. A., and A. Folguera (2009), Andean flat-slab subduction through time, in *Ancient Orogens and Modern Analogues, Special Publication*, vol. 327, edited by Murphy, J. B., et al., pp. 31–54, Geol. Soc., London, doi:10.1144/SP327.3.
- Ranero, C., and V. Sallares (2004), Geophysical evidence for hydration of the crust and mantle of the Nazca plate during bending at the north Chile trench, *Geology*, *32*, 549–552.
- Rawlinson, N., A. Fichtner, M. Sambridge, and M. Young (2014), Seismic tomography and the assessment of uncertainty, *Adv. Geophys.*, *55*, 1–76.
- Rea, D. K., and L. J. Ruff (1996), Composition and mass flux of sediment entering the world's subduction zones: Implications for global sediment budgets, great earthquakes, and volcanism, *Earth Planet. Sci. Lett.*, *140*, 1–12.
- Rüpke, L. H., J. P. Morgan, M. Hort, and J. A. D. Connolly (2004), Serpentine and the subduction zone water cycle, *Earth Planet. Sci. Lett.*, *223*, 17–34.
- Ryan, J., S. Beck, G. Zandt, L. Wagner, and E. Minaya (2016), Central Andean crustal structure from receiver function analysis, *Tectonophysics*, doi:10.1016/0040-1951(96)00024-8.
- Sabra, K. G., P. Gerstoft, P. Roux, W. A. Kuperman, and M. C. Fehler (2005), Surface wave tomography from microseisms in Southern California, *Geophys. Res. Lett.*, *32*, L14311, doi:10.1029/2005GL023155.
- Saygin, E., and B. L. N. Kennett (2010), Ambient seismic noise tomography of Australian continent, *Tectonophysics*, *481*, 116–125.

- Saylor, J. E., and B. K. Horton (2014), Nonuniform surface uplift of the Andean plateau revealed by deuterium isotopes in Miocene volcanic glass from southern Peru, *Earth Planet. Sci. Lett.*, *387*, 120–131.
- Schmidt, M. W., and S. Poli (1998), Experimentally based water budgets for dehydrating slabs and consequence for arc magma generation, *Earth Planet. Sci. Lett.*, *163*, 361–379, doi:10.1016/S0012-821X(98)00142-3.
- Scire, A., G. Zandt, S. Beck, M. Long, L. Wagner, E. Minaya, and H. Tavera (2016), Imaging the transition from flat to normal subduction: Variations in the structure of the Nazca slab and upper mantle under southern Peru and northwestern Bolivia, *Geophys. J. Int.*, *204*, 457–479, doi:10.1093/gji/ggv452.
- Shapiro, N. M., M. Campillo, L. Stehly, and M. H. Ritzwoller (2005), High-resolution surface-wave tomography from ambient seismic noise, *Science*, *307*(5715), 1615–1618, doi:10.1126/science.1108339.
- Shephard, G. E., R. D. Müller, L. Liu, and M. Gurnis (2010), Miocene drainage reversal of the Amazon River driven by plate-mantle interaction, *Nat. Geosci.*, *3*, 870–875, doi:10.1038/NGEO1017.
- Sibson, R. (1980), A vector identity for the Dirichlet tessellation, *Math. Proc. Camb. Philos. Soc.*, *87*, 151–155.
- Sibson, R. (1981), A brief description of the natural neighbor interpolant, in *Interpolating Multivariate Data*, edited by V. Barnett, pp. 21–36, Wiley, Chichester.
- Sobolev, S. V., and A. Y. Babeyko (2005), What drives orogeny in the Andes? *Geology*, *33*, 617–620, doi:10.1130/G21557.1.
- Sobolev, S. V., A. Y. Babeyko, I. Koulakov, and O. Oncken (2006), Mechanism of the Andean orogeny: Insight from numerical modeling, in *The Andes—Active Subduction Orogeny*, *Front. in Earth Sci.*, vol. 1, edited by O. Oncken et al., pp. 513–535, Springer, Berlin.
- Sodoudi, F., X. Yuan, G. Asch, and R. Kind (2011), High-resolution image of the geometry and thickness of the subducting Nazca lithosphere beneath northern Chile, *J. Geophys. Res.*, *116*, B04302, doi:10.1029/2010JB007829.
- Stachnik, J. C., K. Dueker, D. L. Schutt, and H. Yuan (2008), Imaging Yellowstone plume-lithosphere interactions from inversion of ballistic and diffusive Rayleigh wave dispersion and crustal thickness data, *Geochem. Geophys. Geosyst.*, *9*, Q06004, doi:10.1029/2008GC001992.
- Tassara, A., and A. Echaurren (2012), Anatomy of the Andean subduction zone: Three dimensional density model upgraded and compared against global-scale models, *Geophys. J. Int.*, *189*(1), 161–168, doi:10.1111/j.1365-246X.2012.05397.x.
- Ulmer, P., and V. Trommsdorff (1995), Serpentine stability to mantle depths and subduction-related magmatism, *Science*, *268*, 858–861.
- Victor, P., O. Oncken, and J. Glodny (2004), Uplift of the western Altiplano plateau: Evidence from the Cordillera between 20° and 21°S (northern Chile), *Tectonics*, *23*, TC4004, doi:10.1029/2003TC001519.
- Wada, I., K. L. Wang, J. G. He, and R. D. Hyndman (2008), Weakening of the subduction interface and its effects on surface heatflow, slab dehydration, and mantle wedge serpentinization, *J. Geophys. Res.*, *113*, B04402, doi:10.1029/2007JB005190.
- Wagner, L. S., S. Beck, G. Zandt, and M. N. Ducea (2006), Depleted lithosphere, cold, trapped asthenosphere, and frozen melt puddles above the flat slab in central Chile and Argentina, *Earth Planet. Sci. Lett.*, *245*(1), 289–301.
- Wagner, L. S., M. J. Fouch, D. James, and S. Hanson-Hedgecock (2012), Crust and upper mantle structure beneath the Pacific Northwest from joint inversions of ambient noise and earthquake data, *Geochem. Geophys. Geosyst.*, *13*, Q0AN03, doi:10.1029/2012GC04353.
- Wagner, L., D. Forsyth, M. Fouch, and D. James (2010a), Detailed three-dimensional shear wave velocity structure of the northwestern United States from Rayleigh wave tomography, *Earth Planet. Sci. Lett.*, *299*, 273–284.
- Wagner, L., S. Beck, and M. Long (2010b), PerU Lithosphere and Slab Experiment, International Federation of Digital Seismograph Networks. Other/Seismic Network. doi:10.7914/SN/ZD_2010.
- Ward, K. M., R. C. Porter, G. Zandt, S. L. Beck, L. S. Wagner, E. Minaya, and H. Tavera (2013), Ambient noise tomography across the central Andes, *Geophys. J. Int.*, *194*, 1559–1573.
- Ward, K. M., G. Zandt, S. L. Beck, D. H. Christensen, and H. McFarlin (2014a), Seismic imaging of the magmatic underpinnings beneath the Altiplano-Puna volcanic complex from the joint inversion of surface wave dispersion and receiver functions, *Earth Planet. Sci. Lett.*, *404*, 43–53, doi:10.1016/j.epsl.2014.07.022.
- Ward, K., R. C. Porter, G. Zandt, S. L. Beck, L. S. Wagner, E. Minaya, and H. Tavera (2014b), Erratum: Ambient noise tomography across the central Andes, *Geophys. J. Int.*, *196*, 1264–1265.
- Weeraratne, D. S., D. W. Forsyth, Y. Yang, and S. C. Webb (2007), Rayleigh wave tomography beneath intraplate volcanic ridges in the South Pacific, *J. Geophys. Res.*, *112*, B06303, doi:10.1029/2006JB004403.
- Wessel, P., W. H. F. Smith, R. Scharroo, J. F. Luis, and F. Wobbe (2013), Generic mapping tools: Improved version released, *Eos Trans. AGU*, *94*, 409–410, doi:10.1002/2013EO450001.
- Wielandt, E. (1993), Propagation and structural interpretation of non-plane waves, *Geophys. J. Int.*, *113*, 45–53.
- Yang, Y. (2014), Application of teleseismic long-period surface waves from ambient noise in regional surface wave tomography: A case study in western USA, *Geophys. J. Int.*, *198*(3), 1644–1652.
- Yang, Y., and D. W. Forsyth (2006), Regional tomographic inversion of the amplitude and phase of Rayleigh waves with 2-D sensitivity kernels, *Geophys. J. Int.*, *166*, 1148–1160.
- Yang, Y., M. H. Ritzwoller, A. L. Levshin, and N. M. Shapiro (2007), Ambient noise Rayleigh wave tomography across Europe, *Geophys. J. Int.*, *168*(1), 259–274.
- Yang, Y., et al. (2010), Rayleigh wave phase velocity maps of Tibet and the surrounding regions from ambient seismic noise tomography, *Geochem. Geophys. Geosyst.*, *11*, Q08010, doi:10.1029/2010GC003119.
- Yang, Y., W. Shen, and M. H. Ritzwoller (2011), Surface wave tomography on a large-scale seismic array combining ambient noise and teleseismic earthquake data, *Earth Sci.*, *24*, 55–64, doi:10.1007/s11589-011-0769-3.
- Zheng, S. H., X. L. Sun, X. D. Song, Y. J. Yang, and M. H. Ritzwoller (2008), Surface wave tomography of China from ambient seismic noise correlation, *Geochem. Geophys. Geosyst.*, *9*, Q05020, doi:10.1029/2008GC001981.
- Zhou, Y., F. Dahlen, and G. Nolet (2004), Three-dimensional sensitivity kernels for surface wave observables, *Geophys. J. Int.*, *158*, 142–168.